

# GLOBAL PROPERTIES OF THE GLOBULAR CLUSTER SYSTEMS OF FOUR SPIRAL GALAXIES

KATHERINE L. RHODE<sup>1</sup>

Astronomy Department, Wesleyan University, Middletown, CT 06459; kathy@astro.wesleyan.edu

and

Department of Astronomy, Yale University, New Haven, CT 06520

STEPHEN E. ZEPF

Department of Physics & Astronomy, Michigan State University, East Lansing, MI 48824; zepf@pa.msu.edu

ARUNAV KUNDU

Department of Physics & Astronomy, Michigan State University, East Lansing, MI 48824; kundu@pa.msu.edu

AARON N. LARNER

Astronomy Department, Wesleyan University, Middletown, CT 06459; alarner@wesleyan.edu

## ABSTRACT

We present results from a wide-field imaging study of the globular cluster (GC) systems of a sample of edge-on, Sb–Sc spiral galaxies  $\sim 7$ –20 Mpc away. This study is part of a larger survey of the ensemble properties of the GC populations of giant galaxies. We imaged the galaxies in  $BVR$  filters with large-format CCD detectors on the WIYN 3.5-m telescope, to projected radii of  $\sim 20$ –40 kpc. For four galaxies (NGC 2683, NGC 3556, NGC 4157, and NGC 7331), we quantify the radial distributions of the GC systems and estimate the total number, luminosity- and mass-normalized specific frequencies ( $S_N$  and  $T$ ), and blue (metal-poor) fraction of GCs. A fifth galaxy (NGC 3044) was apparently too distant for us to have detected its GC system. Our  $S_N$  for NGC 2683 is 2.5 times smaller than the previously-published value, likely due in part to reduced contamination from non-GCs. For the spiral galaxies analyzed for the survey to date, the average number of GCs is  $170 \pm 40$  and the weighted mean values of  $S_N$  and  $T$  are  $0.8 \pm 0.2$  and  $1.4 \pm 0.3$ . We use the survey data to derive a relationship between radial extent of the GC system and host galaxy mass over a factor of 20 in mass. Finally, we confirm the trend, identified in previous survey papers, of increasing specific frequency of metal-poor GCs with increasing galaxy mass. We compare the data with predictions from a simple model and show that carefully quantifying the numbers of metal-poor GCs in galaxies can constrain the formation redshifts of the GCs and their host galaxies.

*Subject headings:* galaxies: spiral — galaxies: individual (NGC 2683, NGC 3044, NGC 3556, NGC 4157, NGC 7331) — galaxies: star clusters — galaxies: formation

## 1. INTRODUCTION

Much has been learned about the structure and formation of the Milky Way Galaxy from studies of its globular cluster system. The key historical development in this area was Shapley’s use of globular clusters to investigate the structure of the Galaxy and the location of the Solar System within it (e.g., Shapley 1918). Many decades later, Searle & Zinn (1978) made abundance estimates for a subset of Galactic globular clusters and used them to infer a chaotic, hierarchical scenario for the formation of the Galactic halo. Zinn (1985) later identified distinct “halo” and “disk” subpopulations of globular clusters in the Milky Way, having different kinematics, spatial distributions, and, by inference, different origins. To date,  $\sim 150$  globular clusters have been identified in our Galaxy (Harris 1996) and numerous studies have yielded estimates of their distances, abundances, kinematics, and ages; together these provide crucial information regarding the assembly history of the Galaxy. Furthermore, the globular cluster system of the other massive spiral

galaxy in our neighborhood, Andromeda, has been surveyed fairly completely in the past decade, so that we now have estimates of the colors, metallicities, and kinematics of a substantial fraction of its  $\sim 450$  globular clusters (e.g., Barmby et al. 2000; Perrett et al. 2002).

The natural question that arises is whether what we have learned about the globular cluster systems of the Milky Way and Andromeda is true for other galaxies of similar mass, especially spiral galaxies. Are the Milky Way and Andromeda representative of other spiral galaxies, in terms of the total numbers, spatial distributions, colors, and specific frequencies of their globular cluster populations? If the Milky Way and Andromeda globular cluster systems are similar to (or different from) those of other galaxies, what does that tell us about how galaxies form and evolve?

Although studies of extragalactic globular cluster systems have multiplied rapidly over the past decade (see the recent review by Brodie & Strader 2006), observational studies of spiral galaxy GC systems are still comparatively rare. Ashman & Zepf (1998) put together a comprehensive table of the existing data on galaxies’

<sup>1</sup> NSF Astronomy & Astrophysics Postdoctoral Fellow

GC systems (quantities such as total number, specific frequency, and mean metallicity). The table included 82 galaxies, and only twelve were spiral galaxies (Hubble type Sa – Scd), including the Milky Way and M31. Since that time, *Hubble Space Telescope* (*HST*) studies of several more spiral galaxies have been published (e.g., Goudfrooij et al. 2003; Chandar, Whitmore, & Lee 2004). Although the high resolution of *HST* offers distinct advantages in terms of distinguishing GCs from contaminants such as faint background galaxies, its small field of view means that typically only a small subset of the area around the galaxies is observed, which makes it difficult to accurately determine the global properties (spatial and color distributions, total numbers) of the GC systems. For example, we showed in our wide-field imaging study of the GC system of the spiral galaxy NGC 7814 that quantities like the total number and specific frequency of GCs can be off by  $\sim 20$ – $75\%$  when one extrapolates results from *HST* data, or small-format CCD data, out to large radius (Rhode & Zepf 2003 and references therein).

This paper presents results from wide-field CCD imaging of the globular cluster systems of four Sb–Sc spiral galaxies: NGC 2683, NGC 3556, NGC 4157, and NGC 7331. We also discuss observations of a fifth galaxy, the Sc galaxy NGC 3044, which apparently is too distant for us to have detected its GC system. Basic properties of these five galaxies are given in Table 1. The data presented here were acquired as part of a survey that uses large-format and mosaic CCD imagers to study the global properties of the GC systems of spiral, S0, and elliptical galaxies at distances of  $\sim 7$ – $20$  Mpc. A description of the survey, and results for the first five galaxies analyzed, are given in Rhode & Zepf (2001, 2003, and 2004; hereafter RZ01, RZ03, RZ04). Because of difficulties in quantifying the selection effects caused by intrinsic structure and line-of-sight extinction in spiral galaxy disks, the only reliable way to quantify the global properties of spiral galaxy GC populations is to study galaxies that appear edge-on in the sky. Therefore the spiral galaxy targets chosen for the survey have  $i \lesssim 75^\circ$ . We use techniques such as imaging in multiple filters and analyzing archival *HST* data to carefully reduce contamination from non-GCs and estimate the amount of contamination that remains in the samples. Our main goal is to accurately quantify the spatial distribution of each galaxy’s GC system over its full radial range, in order to then calculate a reliable total number of GCs for the system. We can then compare these total numbers to predictions from galaxy formation models such as Ashman & Zepf (1992; hereafter AZ92), who suggested that elliptical galaxies and their GC systems can be formed by the collision of spiral galaxies. Somewhat more generally, we wish to compare the global properties of the GC systems of the spiral galaxies in the survey to those of galaxies of other morphological types (ellipticals and S0s). Making such a comparison will help us determine the typical GC system properties for galaxies of different types, and what that might tell us about galaxy origins in general.

The paper is organized as follows. Section 2 describes the observations and initial data reduction steps. Section 3 explains our methods for detecting GCs and analyzing the GC system properties. Section 4 gives the results, and the final section is a summary of the study.

## 2. OBSERVATIONS & INITIAL REDUCTIONS

Images of the targeted spiral galaxies were taken between 1999 October and 2001 January with the 3.5-m WIYN telescope<sup>2</sup> at Kitt Peak National Observatory. One of two CCD detectors was used; either a single 2048 x 2048-pixel CCD (S2KB) with 0.196'' pixels and a 6.7' x 6.7' field of view, or the Minimosaic Imager, which consists of two 2048 x 4096-pixel CCD detectors with 0.14'' pixels and a total field of view 9.6' x 9.6'. For the four nearest galaxies (with distances 7–15 Mpc), the galaxy was positioned toward the edge of the detector, to maximize the radial coverage of the GC system. NGC 3044 was substantially more distant, at  $>20$  Mpc away, and so was positioned in the center of the detector. A series of images was taken in three broadband filters (*BVR*). Table 2 specifies for each galaxy the dates of the observations, the detector used, and the number of exposures and integration times in each filter.

The images of NGC 3044, NGC 3556, NGC 4157, and NGC 7331 were taken under photometric conditions, and calibrated with observations of photometric standard stars (Landolt 1992) taken on the same nights as the imaging data. The images of NGC 2683 were taken under non-photometric sky conditions. In this case we took single, short (400 – 600 s) *BVR* exposures of the galaxy on a subsequent, photometric night during the same observing run (in January 2001). We used these short exposures along with calibration frames taken on the same night to post-calibrate the longer exposures of NGC 2683.

The photometric calibration data for the five galaxies discussed in this paper were taken on five different nights, with one of two CCD detectors (Minimosaic or S2KB). The color coefficients in the *V* magnitude equation ranged from 0.02 to 0.08, with a typical formal uncertainty of 0.01. The color coefficients in the *B*–*V* color equation ranged from 1.01 to 1.06, with a typical uncertainty of 0.01. The color coefficients in the *V*–*R* color equation ranged from 1.04 to 1.06, with an uncertainty of 0.01 to 0.03. The formal errors on the zero points in the *V*, *B*–*V*, and *V*–*R* calibration equations fell between 0.003 and 0.01, indicating that it was in fact photometric on the nights that the calibration data were taken.

Preliminary reductions (overscan and bias subtraction, flat-field division) were done with standard reduction tasks in the IRAF<sup>3</sup> packages CCDRED (for the S2KB images) or MSCRED (for the Minimosaic images). The MSCRED tasks MSCZERO, MSCMATCH, and MSCIMAGE were used to convert the multi-extension Minimosaic FITS images into single images. The images taken of each galaxy target were aligned to each other, and then sky subtraction was performed on each individual image. The individual images taken with a given filter of a given galaxy target were then scaled to a common flux level and combined, to create a deep, cosmic-ray-free image of each galaxy in each of the three filters. Finally, the sky background level was restored to

<sup>2</sup> The WIYN Observatory is a joint facility of the University of Wisconsin, Indiana University, Yale University, and the National Optical Astronomy Observatories.

<sup>3</sup> IRAF is distributed by the National Optical Astronomy Observatories, which are operated by the Association of Universities for Research in Astronomy (AURA), Inc., under cooperative agreement with the National Science Foundation.

each of the combined images. The resolution (FWHM of the point spread function) of the final combined images ranges from:  $0.6''$  to  $0.9''$  for NGC 2683,  $0.7''$  to  $1.1''$  for NGC 3044;  $0.7''$  to  $1.0''$  for NGC 3556;  $0.9''$  to  $1.1''$  for NGC 4157; and  $0.9''$  to  $1.0''$  for NGC 7814.

### 3. DETECTION & ANALYSIS OF THE GLOBULAR CLUSTER SYSTEM

#### 3.1. Source Detection and Matching

Globular clusters at the distances of our galaxy targets will appear unresolved in ground-based images. To detect GCs, we first removed the diffuse galaxy light from the images. The final combined images were smoothed with a ring median filter of diameter equal to 7 times the mean FWHM of point sources in the image. The smoothed images were then subtracted from the original versions to create a galaxy-subtracted image. (We experimented with filters of varying diameter for the smoothing step and found that the ring filter with the specified diameter consistently removed the diffuse galaxy light without removing any of the light from the point sources.) The appropriate constant sky level was restored to the galaxy-subtracted images and then the IRAF task DAOFIND was used to detect sources with a signal-to-noise level between 3.5 and 6 times the noise in the background. We masked out the high-noise regions of the galaxy-subtracted images where pointlike GC candidates could not reliably be detected, such as the inner, dusty disks of the galaxies and regions immediately surrounding saturated foreground stars or large resolved background galaxies. We removed from the DAOFIND lists any sources located within these masked regions, and then matched the remaining sources to produce a final list of sources detected in all three filters. The number of sources remaining after this step was 537 in NGC 2683, 522 in NGC 3044, 573 in NGC 3556, 387 in NGC 4157, and 304 in NGC 7331.

#### 3.2. Eliminating Extended Sources

To remove extended objects (e.g., contaminating background galaxies) from the source lists, we began by measuring the FWHM of each source in the matched lists and plotting it versus its instrumental magnitude. An example of such a plot is Figure 1, which shows FWHM vs. magnitude for the 387 detected sources in the  $V$  and  $R$  images of NGC 4157. At bright magnitudes, point sources have FWHM values that form a tight sequence around some mean value. Extended objects have larger FWHM values, scattered over a larger range. At fainter instrumental magnitudes, point sources still scatter around the same mean value, but their FWHM values spread out; consequently, the border between the FWHM values of point sources and extended objects becomes less clear at faint magnitudes.

We created FWHM vs. instrumental magnitude plots for the final combined images of each galaxy, and then eliminated extended objects by selecting as GC candidates only those sources with FWHM values close to the mean FWHM value of point sources for each image. We visually examined the plots to determine the boundary between point sources and extended objects, and then wrote a computer code to implement the extended source cut. The range of acceptable FWHM values gradually

increases with increasing magnitude of the sources. We used the FWHM information in the different filters independently (i.e., if a source had a large FWHM value in *one* of the combined images, it was removed from the GC candidate lists). For NGC 2683 and NGC 7331, we used measurements in all three broadband filters to determine whether a source was extended. For the other three galaxies (NGC 3044, NGC 3556, and NGC 4157), we used measurements from the  $V$  and  $R$  images only, since they had better resolution than the  $B$ -band images and the FWHM versus magnitude plots showed significantly less scatter in those filters compared to the plot made from the  $B$  image.

Figure 1 shows typical results from this source selection step; objects that are deemed point sources in the  $V$  and  $R$  images of NGC 4157 are plotted with filled circles; objects deemed extended are plotted with open squares. The number of sources remaining after this step was 271 in NGC 2683, 179 in NGC 4157, 275 in NGC 3556, 262 in NGC 3044, and 245 in NGC 7331.

#### 3.3. Photometry

Before doing photometry of the objects in the source lists, we computed individual aperture corrections for each image of each galaxy by measuring the light from 10–20 bright stars within a series of apertures from 1 to 6 times the average FWHM of the image. The aperture corrections are listed in Table 3 and represent the mean difference between the total magnitude of the bright stars and the magnitude within the aperture with radius one FWHM. Photometry with an aperture of radius equal to the average FWHM of the images was then performed for each of the sources that remained after the extended source cut. Calibrated  $BVR$  magnitudes were derived for each source by taking the instrumental magnitude and applying the appropriate aperture correction and photometric calibration coefficients. Corrections for Galactic extinction, derived from the reddening maps of Schlegel et al. (1998), were also applied to produce final  $BVR$  magnitudes. Galactic extinction corrections are listed in Table 4.

#### 3.4. Color Selection

The last step in selecting GC candidates is to choose from the list of point sources the objects with  $V$  magnitudes and  $BVR$  colors consistent with their being GCs at the distance of the host galaxy. This was executed following the same basic steps for all the galaxies. First, objects with  $M_V < -11$  (assuming the distance moduli given in Table 1) were removed from the lists. Then, if an object had a  $B - V$  color and error that put it in the range  $0.56 < B - V < 0.99$ , it was selected. (This  $B - V$  range corresponds to  $[\text{Fe}/\text{H}]$  of  $-2.5$  to  $0.0$  for Galactic GCs; Harris 1996.) Finally, if the objects had  $V - R$  colors and errors that put them within a specified distance from the relation between  $B - V$  and  $V - R$  for Milky Way GCs, they were selected as GC candidates.

In practice, small refinements to this basic set of selection criteria were applied to produce the final list of GC candidates. When the colors of the objects that pass the extended source cut are plotted in the  $BVR$  color-color plane, a marked overdensity of sources in the region of the plane occupied by Galactic GCs is usually obvious. We therefore adjusted the selection criteria slightly to

ensure that all the objects within these “overdensities” were selected as GC candidates. Furthermore, because there are relatively few GC candidates around the spiral galaxies (typically  $<100$ ), we examined each of the objects with magnitudes and colors anywhere close to those of Galactic GCs, to confirm that we were not missing real GCs or (conversely) including likely contaminants in the GC candidate samples.

For NGC 2683, NGC 3044, and NGC 4157, we accepted all objects that were within  $3\sigma$  above or below the  $V - R$  vs.  $B - V$  line for Milky Way GCs (where  $\sigma$  is the scatter in the  $V - R$  vs.  $B - V$  relation). In addition, in NGC 4157, we accepted two sources that were physically located very near the disk of the galaxy and had colors that put them just outside the  $BVR$  selection box, in the direction of the reddening vector. For NGC 7331, we used a  $2\sigma$  criterion for the  $BVR$  color selection in order to exclude several likely contaminants, and we accepted three objects near the galaxy disk with  $BVR$  colors indicating they were probably reddened GCs. For NGC 3556, the overdensity of point sources in the globular cluster region of the  $BVR$  color-color plane was weighted toward the blue side of the  $V - R$  vs.  $B - V$  relation for Milky Way GCs. Therefore for this galaxy, we selected objects that were  $1.5\sigma$  above (redder than) the  $V - R$  vs.  $B - V$  relation, and  $3\sigma$  below (bluer than) the relation. After examining the objects selected in the  $BVR$  color-color plane, we decided to also apply a  $V$  magnitude cut for two of the galaxies, in order to eliminate what appeared to be a significant number of faint background objects that had not been removed in the extended source cut. We excluded objects with  $V > 23.0$  in NGC 2683, and  $V > 23.5$  in NGC 3556 which is, respectively, approximately 0.9 mag and 0.4 mag past the peak of the GC luminosity function in those galaxies. After all of these magnitude and color selection criteria were applied, the final numbers of GC candidates found in NGC 2683, NGC 3556, NGC 4157, and NGC 7331 was 41, 50, 37, and 37, respectively.

NGC 3044 was a special case. When we plotted the 262 point sources detected around this galaxy in the  $BVR$  color-color plane, it was immediately apparent that there was no overdensity of objects in the part of the plane occupied by GCs. We nevertheless applied a typical set of color selection criteria — i.e.,  $B - V$  in the usual range and  $V - R$  within  $3\sigma$  above or below the expected value for Galactic GCs — and created a list of 35 possible GC candidates, with  $V = 20.9 - 24.4$ . These objects were spread uniformly over the field of view of the WIYN images, rather than being strongly clustered around the galaxy, as is typical for the other spiral galaxy GC systems we have surveyed. Only 2 of the 35 objects with GC-like magnitudes and colors were located within a projected radius of 2.2 arc minutes (15 kpc, assuming the 23 Mpc distance) from the galaxy center. (In the Milky Way, more than 80% of the catalogued GCs have projected radial distances of 15 kpc or less; Harris 1996.) This suggests that the GC system of NGC 3044 was not clearly detected with our WIYN observations. Assuming that this galaxy’s distance modulus is 31.83 and that its GCLF peaks at  $M_V = -7.33$  like the Milky Way GCLF (Ashman & Zepf 1998), the GCs in the luminous half of the GCLF should have  $V$  magnitudes in the range 20.8–24.5. The survey images are typically

50% complete at  $B$ ,  $V$ , and  $R$  magnitudes of 24–25 (see Section 3.5), so many such luminous GCs should be detectable in the images. It may be that this galaxy has a  $S_N$  significantly lower than those of the Milky Way and the other spiral galaxies in our survey (and thus has very few luminous GCs), that the galaxy actually lies somewhat further away than 23 Mpc, and/or that the magnitude limits of the images and our selection techniques prevent us from detecting the GCs that are there. In any case, because no convincing GC candidates were detected in NGC 3044, no further analysis steps were executed for this galaxy.

Figures 2 through 6 illustrate the results of the color selection; objects appearing as point sources in the WIYN images are shown as open squares, and filled circles are the final selected GC candidates. We include the  $BVR$  color-color plots for NGC 3044 for completeness. Note that because of the  $V$  magnitude criteria applied, some objects within the color selection boxes are not selected as GC candidates. For illustrative purposes, the figures show the expected locations of galaxies of different morphological types, at different redshifts. The “galaxy tracks” were produced by taking template galaxy spectra for early- to late-type galaxies, shifting the spectra to simulate moving the galaxies to redshifts between 0 and 0.7, and then calculating their  $BVR$  colors (see RZ01 for details). The galaxy tracks simply show that late-type, low- to moderate-redshift galaxies have  $BVR$  colors similar to GCs, so not every GC candidate in the samples at this stage is a real GC; some may be background galaxies. (Section 3.6 details our efforts to quantify the amount of contamination in the GC candidate lists.)

Figure 7 shows color-magnitude diagrams for the GC candidates in the four galaxies in which the GC system was detected. The  $V$  magnitudes of the GC candidates are plotted versus their  $B - R$  colors. The final numbers of GC candidates found in the galaxies are marked on the plots.

### 3.5. Completeness Testing

A series of completeness tests was done to determine the point-source detection limits of the WIYN images of each galaxy. We began by adding artificial point sources with magnitudes within 0.2 mag of a particular mean value to each of the  $B$ ,  $V$ , and  $R$  images. The number of artificial sources depended on the size of the images: 200 sources were added to the Minimosaic images and 50 were added to the S2KB images (which cover one-fourth the area of the Minimosaic frames). Next, the same detection steps performed on the original images were performed on the images containing the artificial stars, and the fraction of artificial stars recovered in the detection process was recorded. The process was repeated 25–30 times for each image, incrementing the mean magnitude of the artificial stars by 0.2-mag each time, so that the completeness was calculated over a range of 5–6 magnitudes for each filter, for each galaxy. Table 5 lists the 50% completeness limits for the three filters for each galaxy.

### 3.6. Quantifying and Correcting for Contamination

Some fraction of the objects chosen as GC candidates are actually contaminating objects — that is, foreground stars or background galaxies that have  $BVR$  magnitudes and colors like globular clusters. We used a combination

of techniques to estimate the amount of contamination from non-GCs that existed in our samples, so that we could correct for this contamination in subsequent analysis steps.

### 3.6.1. Contamination Estimate Based on the Asymptotic Behavior of the Radial Profile

Our first step for this set of galaxies was to use the observed radial distribution of GC candidates to help estimate the contamination level. First, an initial radial profile of the GC system of each galaxy was constructed by assigning the GC candidates to a series of annuli, each  $1'$  in width. (More details about the construction of the radial distributions are given in Section 4.1.) The effective area of each annulus (the region where GCs could be detected) was determined and used to calculate a surface density of GC candidates for the annulus. The resultant surface density profile for each galaxy's GC system followed the general shape expected for GC systems, but rather than going to zero in the outer regions, the profiles decreased until reaching a constant positive value in the last few annuli. We assumed this constant surface density was due to contaminating objects (stars and galaxies). We calculated the weighted mean surface density of objects in these outer annuli and took this as an estimate of the contamination level of the GC candidate lists.

For NGC 2683, the initial radial profile created at this step flattened to a constant value in the outer six annuli (of a total of nine annuli). The mean surface density of objects in these outer six annuli is  $0.226 \pm 0.026 \text{ arcmin}^{-2}$ . For NGC 3556, a constant surface density of GC candidates was present in the outer four of eight annuli. Here the level was  $0.093 \pm 0.003 \text{ arcmin}^{-2}$ . For NGC 4157, the situation was more complicated. The initial radial distribution of GC candidates showed typical behavior in the inner few annuli (beginning at some maximum surface density value and then monotonically decreasing with increasing radius) but then showed a “bump” of increased surface density in two adjacent bins in the outer profile, at  $\sim 30 \text{ kpc}$  from the galaxy center. This feature in the radial profile is caused by a group of GC candidates in the halo of the galaxy and is discussed in detail in Section 4.1. The objects may be *bona fide* GCs in the galaxy's outer halo, or a distant, background cluster of galaxies masquerading as GCs, or just a chance superposition of several otherwise-unrelated GC candidates. In any case, to estimate the surface density of contaminants, we removed the seven closely-grouped GC candidates responsible for the inflated surface density in those two outer bins, and calculated the mean surface density of GC candidates in the outer five (of nine total) annuli. The estimated surface density of contaminants from this analysis is  $0.181 \pm 0.059 \text{ arcmin}^{-2}$ . Finally, for NGC 7331, the images covered less area around the galaxy, so the radial coverage of the GC system was reduced. The initial radial profile of GC candidates flattened in the outer two (of five) annuli and the average surface density in these annuli is  $0.690 \pm 0.220 \text{ arcmin}^{-2}$ .

### 3.6.2. Estimating Stellar Contamination from a Galactic Star Counts Model

We used the Galactic structure model code of Mendez & van Altena (1996) and Mendez et al. (2000) to yield

an independent estimate of the level of contamination from Galactic stars in the GC candidate lists. Given specific values for variables such as the Galactocentric distance of the Sun and the proportions of stars in the Galaxy halo, disk, and thick disk, the code outputs the predicted number of Galactic stars with  $V$  magnitudes and  $B - V$  colors in a user-specified range, in a given area of the sky. We ran the model for each of our galaxy targets, adjusting the range of  $V$  magnitudes of the Galactic stars to match the  $V$  range of the GC candidates. The model-predicted surface density of stars with  $V$  magnitudes and  $B - V$  colors like the GC candidates in the directions NGC 2683, NGC 3556, NGC 4157, and NGC 7331 were  $0.067 \text{ arcmin}^{-2}$ ,  $0.040 \text{ arcmin}^{-2}$ ,  $0.051 \text{ arcmin}^{-2}$ , and  $0.155 \text{ arcmin}^{-2}$ , respectively. (The stellar surface density in the direction of NGC 7331 is large compared to the other galaxies because this galaxy is at  $-20$  degrees Galactic latitude, significantly closer to the Galactic plane than the other galaxies, which have Galactic latitudes between  $+40$  and  $+65$  degrees.) The surface density values were relatively insensitive to the choice of model parameters for the Galaxy. The surface density values range from  $\sim 20$ – $40\%$  of the total surface density of contaminants estimated from the asymptotic behavior of the radial profile.

### 3.6.3. Estimating the Contamination from Background Galaxies with HST Data

Archival *HST* imaging data<sup>4</sup> were available for some of the target spiral galaxies. Because *HST* can resolve many extended objects that appear as point sources in ground-based imaging, determining whether the WIYN GC candidates are actually galaxies gives us another estimate of the contamination in the WIYN data.

We downloaded all of the available archival *HST* images taken in broadband filters of the targeted galaxies; all of these images were taken with the Wide Field and Planetary Camera 2 (WFPC2). We found images that covered portions of the WIYN pointings of NGC 2683, NGC 3556, and NGC 7331, but no data for NGC 4157. The data sets we analyzed are summarized in Table 6. The table lists: proposal ID; target name (either the name of the galaxy or “Any”, which indicates that the images were taken by WFPC2 while another *HST* instrument was being used for the primary science); total exposure time; distance of the observation from the galaxy center; and filter. “On-the-fly” calibration was applied to the images before they were retrieved from the archive. The STSDAS task GCOMBINE was used to combine individual exposures of the same pointing. The WIYN GC candidates were then located in the WFPC2 images. We used the method of Kundu et al. (1999), who measured the flux from GC candidates in apertures of radius 0.5 pixels and 3 pixels and then calculated the ratio of counts in the large and small apertures. Objects that are extended (and therefore galaxies) have count ratios much larger than those of point sources, since relatively more of their light is contained within the 3-pixel aperture. We confirmed the results from the count-ratio method with visual inspection.

<sup>4</sup> Based on observations made with the NASA/ESA *Hubble Space Telescope*, obtained from the data archive at the Space Telescope Science Institute. STScI is operated by AURA, under NASA contract NAS 5-26555.

For NGC 2683, we analyzed a pointing 0.7 arcmin from the galaxy center, taken in the 606W filter, that turned out to contain none of the WIYN GC candidates. We also analyzed a WFPC2 pointing in the 814W filter, centered 1.9 arcmin from the center of the galaxy. Thirteen of the WIYN GC candidates appear in the WFPC2 field and one of these is an extended object rather than a real GC. The area covered by the WFPC2 image is  $5.527 \text{ arcmin}^2$ , so one estimate of the number density of background galaxies (from these admittedly small-number statistics) is  $0.181 \text{ arcmin}^{-2}$ .

For NGC 3556, there was a WFPC2 pointing in the 606W filter, located 0.4 arcmin from the galaxy center. Five of the WIYN GC candidates appear in the combined WFPC2 image; none is extended.

NGC 7331 had many WFPC2 images available in the HST archive, largely because this galaxy was a target for the HST Cepheid Key Project (Hughes et al. 1998). We made combined images from multiple observations of two different pointings located  $3.5'$  and  $5'$  from the galaxy (see Table 6). Only one of these pointings contained WIYN GC candidates, however; the other pointing happened to coincide with a small area of the WIYN frames that contained no GC candidates. Two of the WIYN GC candidates are located within the WFPC2 pointing at 3.5 arcmin from the galaxy center; neither object is extended.

#### 3.6.4. Final Contamination Correction

For the spiral galaxies here, we will adopt the contamination levels estimated from the asymptotic behavior of the radial profile, and take the Galactic star counts models and HST data analysis as checks on these estimates. NGC 2683 is the one galaxy for which we have independent estimates of the contamination from both stars (from the star counts model) and galaxies (from *HST* data). Adding these two numbers together ( $0.181 \text{ arcmin}^{-2} + 0.067 \text{ arcmin}^{-2}$ ) gives the same number within the errors as the total contamination estimate from the radial profile ( $0.226 \pm 0.026 \text{ arcmin}^{-2}$ ). Also, as noted in Section 3.6.2, the stellar contamination from the Galactic star counts model was always lower than the total contamination estimated from the radial profile, which makes sense if one assumes that galaxies also contribute to the contamination level in the GC candidate samples.

We took the number density of contaminating objects for each galaxy given in Section 3.6.1 and used it to calculate the expected fraction of contaminants at each annulus in the radial profile, for use in subsequent steps. First we multiplied the number density of contaminants by the effective area of the annulus. Dividing this number by the total number of GC candidates in the annulus then yielded the fraction of contaminating objects for that annulus.

#### 3.7. Determining the GCLF Coverage

The observed GC luminosity function (GCLF) was constructed for each of the four galaxies by assigning the  $V$  magnitudes of the GC candidates to bins of width 0.3 mag. The radially-dependent correction described in Section 3.6.4 was used to correct the LF data for contamination. For example, if a GC candidate was located 2 arcmin from the galaxy center and the contamination

fraction was expected to be 20% at that radius, then 0.8 was added to the total number of objects in the appropriate  $V$  magnitude bin. The LF was also corrected for completeness, by computing the total completeness of each  $V$  bin (calculated by convolving the completenesses in all three filters, as detailed in RZ01) and dividing the number of GCs in that bin by the completeness fraction.

We assumed the intrinsic GCLF of the spiral galaxies was a Gaussian function with a peak absolute magnitude like that of the Milky Way GCLF,  $M_V = -7.3$  (Ashman & Zepf 1998). If one applies the distance moduli in Table 1, this  $M_V$  translates to peak apparent magnitudes of  $V = 22.1, 23.1, 23.5,$  and  $23.3$ , for NGC 2683, NGC 3556, NGC 4157, and NGC 7331, respectively. We fitted Gaussian functions with the appropriate peak apparent magnitude and dispersions of 1.2, 1.3, and 1.4 mag to the corrected LF data. Bins with less than 45% completeness were excluded from the fitting process. In a few instances we also excluded one or more bins with very low numbers (e.g., bins containing less than one GC candidate) that were causing the normalization to be too low to fit well to the surrounding bins. The fraction of the theoretical GCLF covered by the observed LF was calculated for each galaxy. The mean fractional coverage (averaged for the three different dispersions) and error for NGC 2683, NGC 3556, NGC 4157, and NGC 7331 were  $0.64 \pm 0.02$ ,  $0.53 \pm 0.02$ ,  $0.513 \pm 0.001$ , and  $0.51 \pm 0.02$ , respectively.

Finally, we experimented with changing the bin size of the LF data and quantified how this affected the final value of the fractional GCLF coverage. We found that changing the bin size produced a change in the mean fractional coverage of 4–7%. This uncertainty is included in the final errors (i.e., the error on specific frequency) on quantities discussed in Section 4.3.

## 4. RESULTS

### 4.1. Radial Distributions of the GC Systems

We constructed radial profiles of the galaxies' GC systems by binning the GC candidates into a series of  $1'$ -wide annuli according to their projected radial distances from the galaxy centers. The inner parts of the spiral galaxy disks had been masked out (see Section 3.1) because GCs could not be reliably detected there; thus the positions of the radial bins were adjusted so that the inner radius of the first annulus started just outside this masked central region. An effective area — the area in which GCs could be detected, excluding the masked portions of the galaxy, masked regions around saturated stars, and parts of the annulus that extended off the image — was computed for each annulus. We corrected the number of GCs in each annulus for contamination (by applying the radially dependent contamination correction described in Section 3.6.4) and for GCLF coverage. The final radial distribution of the GC system was then produced by dividing the corrected number of GCs in each annulus by the effective area of the annulus. The errors on the GC surface density values for each annulus include uncertainties on the number of GCs and contaminating objects. Tables 7 through 10 give the final radial distributions of the GC systems for the four galaxies; the radial profiles are plotted in Figures 8 through 11. The projected radii shown in the tables and figures are

the mean projected radii of the unmasked pixels in each annulus. Note that because a contamination correction has been applied to the surface density of GCs in each radial bin, some of the outer bins have negative surface densities.

We fitted power laws of the form  $\log \sigma_{\text{GC}} = a_0 + a_1 \log r$  and deVaucouleurs laws of the form  $\log \sigma_{\text{GC}} = a_0 + a_1 r^{1/4}$  to the radial distributions. In all cases the  $\chi^2$  values were nearly the same for both the power law and deVaucouleurs law fits, so we list the coefficients for both functions in Table 11. The top panels of Figures 8 through 11 show the surface density of GCs versus projected radius and the bottom panels show the log of the surface density versus  $r^{1/4}$ , with the best-fit deVaucouleurs law plotted as a dashed line.

The GC system radial profiles of each of the galaxies have slightly different appearances, but in all cases the GC surface density decreases to zero within the errors before the last data point. This suggests that we have observed the full radial extent of the galaxies' GC systems, which is crucial for a reliable determination of the total number of GCs in the system. For NGC 2683, the surface density is consistent with zero by a radius of  $4'$ , or  $\sim 9$  kpc. For NGC 3556, which is a much more luminous spiral galaxy, the GC surface density goes to zero at  $5.5'$ , or  $\sim 20$  kpc.

NGC 7331 has the lowest inclination of any spiral galaxy in our survey. (In addition to the current set of galaxies, the survey also includes NGC 7814, published in RZ03, and NGC 891 and NGC 4013, which are not yet published.) Because the galaxy has  $i \sim 75$  degrees (rather than the  $i \sim 80$ – $90$  degrees of the other target galaxies), we had to mask out a relatively large portion of its inner radial region, because we could not reliably detect GCs against the background of the galaxy's dusty spiral disk. Consequently the innermost point in the galaxy's radial profile (Fig. 11) is centered at  $>7$  kpc from the galaxy center. In general, the spiral galaxy GC systems we have studied are fairly concentrated toward the galaxy center (as is true for the Milky Way). This seems to be the case for NGC 7331 as well: outside of the masked galaxy disk region, we barely detect NGC 7331's GC system before the data points in the radial profile flatten to a constant surface density (which we take to be the contamination level in the data; see Section 3.6). In the final version of the radial profile shown in Figure 11, the surface densities in the first three radial bins are positive (although the errors on the surface density at  $3'$  make its lower limit barely consistent with zero). Then the GC surface density goes to zero within the errors in the fourth and fifth radial bins. The fourth radial bin is centered at  $4.8'$  (18 kpc), so we take this as the approximate radial extent of this galaxy's GC system.

NGC 4157 was another special case. The radial profile shows the expected behavior in the inner regions of the GC system: the surface density of GCs decreases monotonically with increasing radius until it is consistent with zero in the radial bins centered at  $5'$  and  $6'$ . However the surface density then increases to positive values in the  $7'$  and  $8'$  radial bins, before returning to zero in the last radial bin at  $9'$ . This "bump" in the outer profile is caused by the presence of seven GC candidates with projected distances of  $\sim 30$  kpc from the galaxy center. The seven

candidates appear in two groups: one close group with three objects at  $r = 31.0$ – $31.7$  kpc, and a group of four objects that are somewhat more spread out, with four objects at  $r = 27$ – $32$  kpc. These grouped objects may be real GCs in NGC 4157's halo, or a distant background group or cluster of galaxies. Alternatively, the objects may just appear near each other by chance.

We thought it possible that some or all of the seven GC candidates in question might be associated with a dwarf galaxy that is being accreted into NGC 4157's halo. For this reason we obtained deep, broadband images of NGC 4157 with the WIYN Minimosaic in March 2005. The combined images have a total integration time of 7.5 hours and reach a surface brightness level of  $V > 27$ , but we found no evidence for a faint dwarf galaxy anywhere in the vicinity of those seven GC candidates.

We fitted deVaucouleurs and power laws to both the original version of the radial profile of NGC 4157's GC system and to a profile with the seven GC candidates at  $\sim 30$  kpc removed. Both fits are shown in Figure 10 and listed in Table 9. With the seven "extra" GC candidates removed, the GC surface density is consistent with zero within the errors by  $5'$ , or 20 kpc.

#### 4.2. Radial Extent of the GC Systems of the Survey Galaxies

With (including these four spiral galaxies) a total of nine galaxies from the wide-field survey now analyzed, we can look for trends in the GC system properties of the overall sample. One quantity that we derive from the radial profiles of the GC systems is an estimate of the radial extent of the systems. For the survey, we take the radial extent to be the point at which the surface density of GCs in the final radial profile becomes consistent with zero (within the errors on the surface density) and stays at zero out to the radial limit of the data. Figure 12 shows the radial extent in kiloparsecs of the GC systems of the nine survey galaxies analyzed to date, plotted against the log of the host galaxy stellar mass. To compute the galaxy masses, we combined  $M_V^T$  for each galaxy with the mass-to-light ratios given in Zepf & Ashman (1993):  $M/L_V = 10$  for elliptical galaxies (NGC 3379, NGC 4406, and NGC 4472)  $M/L_V = 7.6$  for S0 galaxies (NGC 4594),  $M/L_V = 6.1$  for Sab–Sb galaxies (NGC 2683, NGC 4157, NGC 7331, and NGC 7814) and 5.0 for Sbc–Sc galaxies (NGC 3556). The errors on the radial extent values in Figure 12 were calculated by taking into account the errors on the distance modulus assumed for each galaxy, along with the errors on the determination of the radial extent itself (which we took to be equal to the width of one radial bin of the spatial profile). Note also that for the spiral galaxy NGC 4157, we derived the radial extent from the version of the radial profile with the seven "extra" GC candidates discussed in Section 12 removed. The galaxy stellar masses and estimated radial extents are listed in Table 12.

Figure 12 shows that, as might be expected, more massive galaxies generally have more extended GC systems, although with a fair amount of scatter in the relation. We fitted a line and a second-order polynomial to the data in the figure; the best-fit line and curve are, respectively:

$$y = ((57.7 \pm 3.7) x) - (619 \pm 41) \quad (1)$$

and

$$y = ((45.7 \pm 9.5) x^2) - ((985 \pm 217) x) + (5320 \pm 1240) \quad (2)$$

where  $x$  is the radial extent in kpc and  $y$  is  $\log(\text{Mass}/M_\odot)$ . One useful application of the data and best-fit relations is determining how much radial coverage is needed in order to observe all or most of the GC system of a particular galaxy. For example, the field of view of the *HST* Advanced Camera for Surveys (ACS) is  $3.37'$  on a side, which means that the maximum radial range observable with this instrument is  $2.38'$  if the galaxy is positioned at the center of the detector. At the approximate distance of the Virgo Cluster ( $\sim 17$  Mpc), this translates to a maximum projected radial distance of  $\sim 12$  kpc. Therefore if one intends to observe the full radial extent of the GC system of a galaxy placed at the center of the HST ACS field, Figure 12 indicates that one is limited to galaxies with stellar mass  $\log(M/M_\odot) < 11$  (which is less massive than the Milky Way Galaxy). One ACS field would include  $\sim 50\%$  of the radial extent of a GC system of a Virgo Cluster galaxy with  $\log(M/M_\odot)$  in the range 11.1–11.2. As explained in Section 1 of this paper and in other papers from the survey (e.g., RZ01, RZ03, RZ04), deriving accurate global values for the properties of a GC system requires that one observe most or all of the radial extent of the system.

#### 4.3. Total Number and Specific Frequency of GCs

The number of GCs in each galaxy can be derived by integrating the deVaucouleurs profiles fitted to the radial distributions (see Section 4.1) out to some outer radial limit. Since the radial distributions are corrected for magnitude incompleteness, missing spatial coverage, and contamination from non-GCs, the result is a final estimate of the total number of GCs in the system ( $N_{GC}$ ). We chose the outer radius of integration to be the point in the radial distribution at which the surface density of GCs equals zero within the errors, and then remains consistent with zero for the remainder of the data points. Note that for NGC 4157, we integrated the deVaucouleurs profile that was fitted to the radial profile with the seven “extra” GC candidates located in the 7–8' bins removed. The outer radius of integration in that case was 5', because with those seven objects removed, the GC surface density is consistent with zero beginning with the 5' bin out to the last bin at 9'.

Given that we could not observe some portion of the inner galaxy — close to the spiral disk — for all four target galaxies, we also had to make assumptions about the number of GCs and/or the shape of the GC radial profile within that region. The projected outer radial boundary of the unobserved region ranged from 0.5–1.3', which translates to 1–5 kpc given the distances to the target galaxies. We assumed four different possibilities for the behavior of the GC systems in these inner regions: (1) that the same proportion of GCs was located within the region as in the Milky Way GC system; (2) that the proportion of GCs missing was like the GC system of NGC 7814 (which we did observe to small radius, with HST WFPC2; see RZ03); (3) that the best-fit deVaucouleurs law profile continued all the way to  $r = 0$ ; and (4) that the inner part of the GC radial distribution was flat (i.e., the GC surface density in the unobserved region

equalled the value in the first radial bin of the observed profile). Adding the number of GCs in the observed part of the system (calculated from integrating the deVaucouleurs profile over the radial range of the data) to the number of GCs in the inner region (given these various assumptions) yielded a range of values for the total number of GCs in each galaxy's system. We took the mean of this range of values as the final estimate of  $N_{GC}$ .

The luminosity- and mass-normalized numbers of GCs in a galaxy are useful quantities to calculate and compare among galaxies. The specific frequency,  $S_N$  was defined by Harris & van den Bergh (1981) as

$$S_N \equiv N_{GC} 10^{+0.4(M_V + 15)} \quad (3)$$

The  $M_V$  values assumed for the galaxies are those given in Table 1. An alternative quantity,  $T$ , was introduced by Zepf & Ashman (1993) and is sometimes preferred to  $S_N$  because it normalizes the number of GCs by the stellar mass of the galaxy ( $M_G$ ) rather than  $V$ -band magnitude:

$$T \equiv \frac{N_{GC}}{M_G / 10^9 M_\odot} \quad (4)$$

To calculate  $M_G$ , we again combined  $M_V^T$  for each galaxy with mass-to-light ratios from Zepf & Ashman (1993). The total numbers,  $S_N$  and  $T$  values for each galaxy's GC system are given in Table 13.

To calculate the errors on  $N_{GC}$  and the specific frequencies  $S_N$  and  $T$ , we took into account the following sources of uncertainty: (1) the variation in the total number of GCs, depending on what was assumed for the spatial distribution of the unobserved inner portion of the GC system; (2) the variation in the calculated coverage of the GCLF, depending on the assumed intrinsic GCLF function and how the luminosity function data were binned; and (3) Poisson errors on the number of GCs and the number of contaminating objects. For NGC 4157, we also estimated the uncertainty in  $N_{GC}$  due to the group of seven GC candidates in the galaxy's halo, and whether these were real GCs (and should therefore be included in the total number) or contaminants. Errors on the specific frequencies  $S_N$  and  $T$  also include uncertainties in the total galaxy magnitudes: we assumed that the internal extinction correction (and thus the galaxy magnitude) could be uncertain by as much as 0.3 mag, which corresponds to 3–4 times the error on  $V_T^0$  given in RC3 (de Vaucouleurs et al. 1991). Individual errors from the above sources were added in quadrature to calculate the final errors on  $N_{GC}$ ,  $S_N$  and  $T$ ; the errors are given in Table 13.

The GC system of one of our targets, NGC 2683, was studied previously by Harris et al. (1985). They used photographic data from the Canada-France-Hawaii telescope to identify  $\sim 100$  GC candidates and estimated that the total number of GCs in NGC 2683 is  $321 \pm 108$ . Combining this number with our assumed  $M_V^T$  value of  $-20.5$  yields a specific frequency  $S_N$  of  $2.0 \pm 0.7$ . This is 2.5 times larger than our measured  $S_N$  value ( $0.8 \pm 0.4$ ). It is not unusual for our survey data to yield smaller  $N_{GC}$  and  $S_N$  values than previous studies; of six galaxies (including NGC 2683) with  $S_N$  values already in the literature, four have previously-published  $S_N$  values significantly larger than those we derive (RZ01, RZ03, RZ04). Our smaller  $S_N$  values are probably due to a combination



of factors, e.g., lower contamination levels (due to source selection in multiple filters and higher resolution data) and more accurate radial distributions yielding better-determined total numbers of GCs.

One of the objectives of our wide-field CCD survey was to determine whether the two spiral galaxies with the most thoroughly studied GC systems, the Milky Way and M31, are typical of their galaxy class in terms of the properties of their GC systems. Figure 13 addresses this question by comparing the luminosity- and mass-normalized specific frequencies of the Milky Way and M31 with those of the spiral galaxies from our survey. The specific frequencies of the five galaxies we have analyzed are plotted with filled circles. Besides the four spiral galaxies presented in this paper, this includes the Sab galaxy NGC 7814 (RZ03). The five spiral galaxies we have analyzed have morphological types of Sab (N=1 galaxy), Sb (N=3), and Sc (N=1) and stellar masses in the range  $\log(M/M_\odot) = 10.9\text{--}11.4$ . Open stars in Figure 13 indicate  $S_N$  and  $T$  for the Milky Way (smaller error bars) and M31. The Milky Way has  $N_{GC} \sim 180$ ,  $S_N = 0.6 \pm 0.1$ , and  $T = 1.3 \pm 0.2$  (Ashman & Zepf 1998). M31 has  $\sim 450$  GCs,  $S_N = 0.9 \pm 0.2$  and  $T = 1.6 \pm 0.4$  (Ashman & Zepf 1998; Barmby et al. 2000). The seven spiral galaxies in the figure show a fairly small range of specific frequency values, with modest scatter (note that  $S_N$  can range from less than zero to  $>10$  for giant galaxies; Ashman & Zepf 1998). The weighted mean  $S_N$  and  $T$  values for the GC systems of the five spiral galaxies in the survey are  $0.8 \pm 0.2$  and  $1.4 \pm 0.3$ , respectively. These values fall between, and are consistent with, the  $S_N$  and  $T$  values for the GC systems of the Milky Way and M31, which suggests that the spiral galaxies we are most familiar with are indeed representative of the GC systems of other spiral galaxies of similar mass, at least in terms of the relative number of GCs. The mean  $N_{GC}$  of the five spiral galaxies we have surveyed to date is  $170 \pm 40$ .

Goudfrooij et al. (2003) analyzed the GC systems of six nearby edge-on spiral galaxies with HST WFPC2 optical imaging data. For five of the galaxies, they had a single WFPC2 observation positioned near the galaxy center; for the sixth galaxy, they had two WFPC2 fields on each side of the disk. Given the distances to their target galaxies, the WFPC2 pointings provided radial coverage of the GC systems out to (typically)  $\sim 5\text{--}15$  kpc. To calculate total numbers and specific frequencies of GCs in the target galaxies, they follow a technique from Kissler-Patig et al. (1999) and compare the numbers of GCs detected in the WFPC2 data with the numbers that would be detected at the same spatial location in the Milky Way GC system if it were observed under the same conditions (i.e., at the same distance and projected onto the sky in the same manner). The mean  $S_N$  value for the five Sab–Sc spiral galaxies studied by Goudfrooij et al. is  $0.96 \pm 0.26$  and the mean  $T$  value is  $2.0 \pm 0.5$ .

Chandar et al. (2004) used HST WFPC2 imaging to study the GC systems of five low-inclination spiral galaxies. They had very limited spatial coverage of the galaxies' GC systems: usually the data consisted of  $\sim 1\text{--}4$  WFPC2 pointings located within the inner  $5'$  ( $<14$  kpc) of each galaxy's disk. To correct for their missing spatial coverage, Chandar et al. (2004) used a technique similar to the one used by Kissler-Patig et al. (1999) and Goudfrooij et al. (2003): they compared the locations of

GCs in their observed fields to the analogous locations and fields in the Milky Way GC system, if it were observed face-on. They calculated a scale factor (equal to the ratio of the number of GCs in the analogous Milky Way region to the number of GCs detected in their observed fields) and applied it to the total number of GCs in the target galaxy. As Goudfrooij et al. and Chandar et al. both note, the implicit assumption in this method is that GC systems of other spirals have the same spatial distributions as that of the Milky Way. For the five spiral galaxies in the Chandar et al. study, the average  $S_N$  is  $0.5 \pm 0.1$  and average  $T$  is  $1.3 \pm 0.2$ .

The mean  $S_N$  and  $T$  values found by Goudfrooij et al. and Chandar et al. are consistent, within the errors, with the average  $S_N$  and  $T$  values we derive from observing the majority of the radial extent of the GC systems. This is perhaps not entirely unexpected, because our mean  $S_N$  and  $T$  values are in line with the corresponding values for the Milky Way, and the *HST* studies necessarily had to assume similarity with the Milky Way GC system in order to calculate their total numbers and specific frequencies.

#### 4.4. Number of Blue (Metal-Poor) GCs Normalized by Galaxy Mass

Another specific objective of the overall wide-field GC system survey is to test a prediction of AZ92, who suggested that elliptical galaxies and their GC populations can form from the merger of two or more spiral galaxies. In the AZ92 model, the GCs associated with the progenitor spiral galaxies form a metal-poor GC population in the resultant elliptical, and a second, comparatively metal-rich population of GCs is formed during the merger itself. For simple stellar populations older than  $\sim 1\text{--}2$  Gyr, broadband colors primarily trace metallicity, with bluer colors corresponding to lower metallicities and red to higher metallicities (see, e.g., Ashman & Zepf 1998). AZ92 therefore predicted that giant elliptical galaxies should show at least two peaks in their broadband color distributions, due to the presence of the metal-poor (blue) GCs associated with the original spiral galaxies and metal-rich (red) GCs formed in star formation triggered by the merger. Bimodal GC color distributions have subsequently been observed in many elliptical galaxies (e.g., Zepf & Ashman 1993, Kundu & Whitmore 2001; Peng et al. 2006). (A detailed discussion of the exact relationship between color and metallicity for old stellar populations in different broadband colors — and whether the bimodal color distributions of elliptical galaxy GC systems really are due to the presence of distinct GC subpopulations — is beyond the scope of this paper. Thorough discussion of these issues is given in, e.g., Zepf (2007), Strader et al. (2007), and Kundu & Zepf (2007).) A consequence of the AZ92 scenario is that the mass-normalized specific frequencies of blue, metal-poor GCs in spiral and elliptical galaxies should be about the same. Our survey data allow us to calculate this quantity,  $T_{\text{blue}}$ , and compare it for galaxies of different morphological types. We define  $T_{\text{blue}}$  as

$$T_{\text{blue}} \equiv \frac{N_{GC}(\text{blue})}{M_G/10^9 M_\odot} \quad (5)$$

where  $N_{GC}(\text{blue})$  is the number of blue GCs and  $M_G$  is

the stellar mass of the host galaxy, calculated by combining  $M_V^T$  with  $M/L_V$ , as described in Section 4.2.

Estimating the proportion of blue GCs in the early-type galaxies from the survey is fairly straightforward because of the large numbers (hundreds to thousands) of GC candidates detected in these galaxies. We make this estimate by first constructing a sample of GC candidates that is at least 90% complete in all three of our imaging filters ( $B$ ,  $V$ , and  $R$ ), creating a GC color distribution from the complete sample, and then running a mixture-modeling code to fit Gaussian functions and estimate the proportion of GCs in the blue and red peaks. The code we use, called KMM (Ashman, Bird, & Zepf 1994), requires at least 50 objects (given the typical color separation between metal-poor and metal-rich GC systems) to produce reliable results.

Calculating  $T_{\text{blue}}$  for the spiral galaxies is more uncertain because of poor statistics: we typically detect tens of GC candidates in the galaxies, and end up with very few objects in the sample of candidates that is complete in  $B$ ,  $V$ , and  $R$ . For NGC 2683, NGC 3556, NGC 4157, and NGC 7331, there were 38, 31, 7, and 26 objects in the complete sample used to construct the GC color distribution. Because we are interested in testing whether the blue GC populations in elliptical galaxies could have originated in spiral galaxies, we define as “blue” those GCs with  $B - R < 1.23$ , the typical location of the separation between the blue and red GC populations in elliptical galaxies (RZ01, RZ04). The percentage of GC candidates with  $B - R < 1.23$  in the complete samples constructed for NGC 2683, NGC 3556, NGC 4157, and NGC 7331 were 63%, 55%, 57%, and 31%. We took these percentages to be lower limits on the percentage of blue GCs for the overall system, since presumably some GCs we detect might be reddened due to internal extinction. Since it seems unlikely that *all* of the GC candidates in the complete sample are reddened and belong in the blue category, we assumed that, at most, 70% of the candidates might be blue. We based this number on the GC systems of the Milky Way and M31, which both show two peaks in their color and metallicity distributions. Roughly 70% of the Milky Way GCs lie in the metal-poor peak (Harris 1996). For M31, the proportion is similar. Barmby et al. (2000) estimate from both photometric and spectroscopic metallicities that  $\sim 66\%$  of M31’s GCs lie in the metal-poor peak. Perrett et al. (2002) publish spectroscopic estimates of  $[\text{Fe}/\text{H}]$  for  $>200$  M31 GCs and estimate that 77% are metal-poor.

We converted these lower- and upper-limit blue percentages into  $T_{\text{blue}}$  values (with an associated error) for each galaxy by multiplying them by the galaxy’s total  $T$  value and error. We then averaged the lower- and upper-limit  $T_{\text{blue}}$  values, and their errors, and took that as the final estimate of  $T_{\text{blue}}$  for each galaxy. These values are given in Table 13. We note that preliminary  $T_{\text{blue}}$  values for NGC 2683, NGC 3556, and NGC 4157 were included in Rhode et al. (2005); the values given in the current paper are the same except that the final calculated errors are slightly larger for NGC 2683 and NGC 4157.

The  $T_{\text{blue}}$  values for the nine galaxies analyzed so far as part of this wide-field GC system imaging survey are shown in Figure 14. This is an updated version of a figure initially shown in Rhode et al. (2005). The figure now includes seven early-type galaxies and seven spiral

galaxies: four early-type galaxies and five spiral galaxies from our survey (RZ01, RZ03, RZ04, and the current paper); the Milky Way (Zinn 1985; Ashman & Zepf 1998); M31 (Ashman & Zepf 1998; Barmby et al. 2000; Perrett et al. 2002); and three elliptical galaxies from the literature (NGC 1052 from Forbes et al. 2001; NGC 4374 from Gomez & Richtler 2004; NGC 5128 from Harris, Harris, & Geisler 2004) that meet our criteria for inclusion in the figure. (Namely, that at least 50% of the radial extent of the GC system is observed, and enough information that the total number of GCs and blue fraction could be estimated; see Rhode et al. (2005) for details.) In the figure, circles denote cluster elliptical galaxies, squares mark field E/S0 galaxies, and triangles are spiral galaxies in the field. Filled symbols are used for our survey data, the Milky Way, and M31; data from other studies are shown with open symbols. (The curves in the figure are discussed below.)

One immediately sees from Figure 14 that the  $T_{\text{blue}}$  values for the spiral galaxies we surveyed are relatively uncertain compared to the early-type galaxies, as a direct result of the poor number statistics described earlier. Even with these uncertainties, it is apparent that the typical  $T_{\text{blue}}$  value for spiral galaxies is smaller than that of the more massive cluster elliptical galaxies. The weighted mean  $T_{\text{blue}}$  for the cluster ellipticals is  $2.3 \pm 0.2$ , compared to  $0.9 \pm 0.1$  for the spiral galaxies. This suggests that some other mechanism — besides the straightforward merging of spiral galaxies envisioned by AZ92 — is needed to create massive cluster elliptical galaxies and their GC populations. On the other hand, the  $T_{\text{blue}}$  values of three of the four field E/S0 galaxies in the figure are comparable to those of the spiral galaxies, which suggests that merging spiral galaxies and their GC systems together is sufficient to account for the metal-poor GC populations of some field E/S0 galaxies. Similar conclusions were made in RZ03, RZ04, and Rhode et al. (2005) and still hold here, with (now) finalized estimates of  $T_{\text{blue}}$  for seven spiral galaxies. (We should note here that previous authors have compared *total* GC specific frequency values for elliptical and spiral galaxies, and reached basically the same result. For example, Harris (1981) compares  $S_N$  for elliptical galaxies in the Virgo cluster and the field to  $S_N$  for the Milky Way, M31, and two other spiral galaxies. Harris (1981) concludes that the merger of disk galaxies with  $S_N < 3$  would produce a new elliptical with  $S_N$  in the range  $\sim 1$  to 3, which is in line with  $S_N$  for some field ellipticals, but much lower than  $S_N$  for Virgo cluster ellipticals.)

Also apparent in Fig. 14 is a general trend of increasing  $T_{\text{blue}}$  value with increasing host galaxy stellar mass: more massive galaxies tend to have proportionally more metal-poor GCs. We first discussed this trend in detail in Rhode et al. (2005) and noted there that it is consistent with a biased, hierarchical galaxy formation scenario such as that suggested by Santos (2003). In this picture, the first generation of GCs form at high redshift during the initial stages of galaxy assembly. The GCs are metal-poor because they form from relatively unenriched gas. This first epoch of GC and baryonic structure formation is then temporarily suppressed at  $z \sim 10-15$ ; Santos (2003) suggests that the suppression is triggered by the reionization of the Universe. Massive galaxies in high-density environments are associated with higher peaks

in the matter density distribution, and therefore began their collapse and assembly process first. The result of such “biasing” is that massive galaxies had assembled a larger fraction of their eventual total mass by the suppression redshift. A larger fraction of their baryonic mass could therefore participate in the formation of the first generation of GCs and as a result, more massive galaxies end up with relatively larger  $T_{\text{blue}}$  values compared to less massive galaxies. Santos (2003) assumes that the break from baryonic structure formation is fairly short-lived ( $<1$  Gyr). During this period, stellar evolution continues to enrich the intergalactic medium, so that any GCs formed after baryonic structure formation resumes will be comparatively metal-rich.

The slope of the expected  $T_{\text{blue}}$  trend depends on the redshift at which the first epoch of GC formation ended. Three curves shown in Fig. 14 illustrate this. The curves come from an extended Press-Schechter calculation (Press & Schechter 1974; Lacey & Cole 1993) done by G. Bryan (private communication). This type of calculation can be used to determine the fraction of mass that is in collapsed halos of a given mass at some early redshift, and that will later end up inside a more massive halo today, at  $z = 0$ . The specific calculation used to create the curves in Fig. 14 assumes that: galaxies are formed via gravitational collapse and assembly of smaller halos that collide and merge together over time; GCs can form within any one of these smaller halos, as long as the halos have masses of at least  $10^8 M_{\odot}$ ; the number of metal-poor GCs that forms is directly proportional to the fraction of a galaxy’s mass that has collapsed by a given redshift; and half the baryons within a given galaxy halo will end up in the form of stars. A constant mass-to-light ratio was used to convert the final total mass of each halo to a stellar mass, for the figure. A  $\Lambda$ CDM cosmology was assumed, with  $\Omega_m = 0.3$ ,  $\Omega_{\Lambda} = 0.7$ ,  $\Omega_b h^2 = 0.02$ ,  $h = 0.65$ , and  $\sigma_8 = 0.9$ . Given these assumptions, the relative number of metal-poor GCs within a given galaxy at  $z = 0$  depends on the redshift at which the metal-poor GCs ceased to form. Fig. 14 shows the predicted  $T_{\text{blue}}$  trend for three different truncation redshifts:  $z = 7$ , 11, and 15. The observed trend seems to fall (very roughly) between the predicted trends for  $z_{\text{form}} > 11$  and  $z_{\text{form}} > 15$ . Much more extensive simulations are needed in order to make rigorous predictions for the relative numbers of metal-poor GCs — and how these numbers depend on the redshift of GC formation — in galaxies over a range of masses, environments, and merger/accretion histories.

Although the curves shown in the figure come from a fairly straightforward calculation with several simplifying assumptions, they show that in principle, a trend in  $T_{\text{blue}}$  such as we have observed is generally consistent with a biased, hierarchical galaxy formation scenario combined with the idea that the first generation of GCs forms within a finite period in the early history of the Universe. We should note here two factors that may influence the apparent relationship between  $T_{\text{blue}}$  and galaxy stellar mass; these are discussed in more detail in RZ04 and Rhode et al. (2005). We used the constant  $M/L_V$  value from Zepf & Ashman (1993) to calculate the stellar mass  $M_G$  for the elliptical galaxies. (For the spiral galaxies,  $M/L_V$  in Zepf & Ashman (1993) changes with morphological type.) In actuality,  $M/L_V$

may have a luminosity dependence as steep as  $L^{0.10}$  (Zepf & Silk 1996 and references therein). As we concluded in RZ04 and Rhode et al. (2005), such a dependence is not sufficient to explain the observed  $T_{\text{blue}}$  trend. Destruction of GCs through dynamical effects (e.g., dynamical friction, evaporation, tidal shocks) may also affect the observed  $T_{\text{blue}}$ -galaxy mass relation. For example, Vesperini (2000) find that destruction may be more efficient in lower-mass galaxies, although this is dependent on the details of how galaxy potentials vary as a function of galaxy mass (e.g., Fall & Zhang 2001). We note finally that relatively few moderate- and high-luminosity galaxies are included in Fig. 14 and that filling in the sparsely-populated regions of the figure would be useful for helping to determine the amount of “biasing” that may be reflected in today’s metal-poor GC populations. We plan to continue our work on measuring global properties and total numbers of GC systems of galaxies with a range of luminosities, morphologies, and environments; with  $T_{\text{blue}}$  values for dozens of galaxies on a figure like Fig. 14, we can more strongly constrain the redshift of formation of the first generation of GCs and their host galaxies.

## 5. SUMMARY

As part of a larger survey that uses wide-field CCD imaging to study the GC systems of giant galaxies, we have acquired and analyzed WIYN *BVR* imaging data of five nearly edge-on spiral galaxies: NGC 2683, NGC 3044, NGC 3556, NGC 4157, and NGC 7331. Our results are as follows:

1. We unequivocally detect the GC systems of all the galaxy targets except the Sc galaxy NGC 3044. Given the magnitude depth of our images, our inability to detect NGC 3044’s GC system may suggest that the galaxy has a low  $S_N$ , or that it lies beyond the 23 Mpc distance estimated from its recession velocity.

2. We observed the GC systems of the target galaxies to projected radial distances of  $\sim 6$ –9 arc minutes (corresponding to 20–40 kpc, depending on the distance to the galaxy) from the galaxy centers. The GC surface density in our derived radial distributions vanishes before the last data point, suggesting that we have observed the full radial extent of the galaxies’ GC systems.

3. The projected radial extents of the GC systems of the target spiral galaxies range from  $\sim 10$ –20 kpc. Combining the current data set with measurements for five other spiral, elliptical, and S0 galaxies from the survey, we derive a coarse relationship between host galaxy mass and radial extent of the GC system. Such a relationship is valuable for planning observations in which the aim is to observe all or most of the spatial extent of a galaxy’s GC system.

4. The estimated total numbers of GCs in the spiral galaxies analyzed for this survey range from  $\sim 80$ –290; the mean  $N_{GC}$  is  $170 \pm 40$ . One of the galaxies presented here, NGC 2683, had a previously-published  $S_N$  value that is 2.5 times larger than our measured value. The weighted mean  $S_N$  and  $T$  values for the five spiral galaxies in the survey are, respectively,  $0.8 \pm 0.2$  and  $1.4 \pm 0.3$ . These values are consistent with the corresponding values for the Milky Way and M31, which suggests that the spiral galaxies with the most thoroughly studied GC systems are representative of the GC systems of other giant

spiral galaxies with similar masses, at least in terms of their relative numbers of GCs.

5. We estimate the galaxy-mass-normalized specific frequency of blue (metal-poor) GCs ( $T_{\text{blue}}$ ) in each galaxy and then combine these results with other data from the survey and the literature. The data confirm our initial conclusion (based on fewer points) that the metal-poor GC populations in luminous ellipticals are too large to have formed via the straightforward merger of two or more spiral galaxies and their associated metal-poor GC populations. The data likewise confirm that  $T_{\text{blue}}$  generally increases with host galaxy mass. By comparing the  $T_{\text{blue}}$  vs. galaxy mass data to results from a simple model, we show that the observed trend is generally consistent with the idea that the first generation of GCs formed in galaxies over a finite period, prior to some truncation redshift.

The research described in this paper was supported by an NSF Astronomy and Astrophysics Postdoctoral

Fellowship (award AST-0302095) to KLR, NSF award AST 04-06891 to SEZ, and NASA Long Term Space Astrophysics grant NAG5-12975 to AK. We are grateful to the Wesleyan University Astronomy Department for funding ANL while he analyzed the data for NGC 7331. We thank Greg Bryan for illuminating discussions and for providing the model calculations shown in Fig. 14. We thank the staff at the WIYN Observatory and Kitt Peak National Observatory for their assistance at the telescope. We also thank Enzo Branchini, who provided some estimated distances for the target galaxies based on a model of the local velocity flow. Finally, we thank the anonymous referee for valuable comments and suggestions that improved the quality of the paper. This research has made use of the NASA/IPAC Extragalactic Database (NED) which is operated by the Jet Propulsion Laboratory, California Institute of Technology, under contract with the National Aeronautics and Space Administration.

#### REFERENCES

- Ashman, K.M., Bird, C.M., & Zepf, S.E. 1994, *AJ*, 108, 2348  
 Ashman, K.M., & Zepf, S.E. 1992, *ApJ*, 384, 50  
 Ashman, K.M., & Zepf, S.E. 1998, *Globular Cluster Systems* (Cambridge: Cambridge University Press)  
 Barmby, P., Huchra, J.P., Brodie, J.P., Forbes, D.A., Schroder, L.L., & Grillmair, C.J. 2000, *AJ*, 119, 727  
 Brodie, J.P. & Strader, J. 2006, *ARA&A*, 44, 193  
 Chandar, R., Whitmore, B., Lee, M.G. 2004, *ApJ*, 611, 220  
 de Vaucouleurs, G., de Vaucouleurs, A., Corwin Jr., H.G., Buta, R.J., Paturel, G., & Fouque, P. 1991, *Third Reference Catalogue of Bright Galaxies* (New York: Springer)  
 Fall, S.M. & Zhang, Q. 2001, *ApJ*, 561, 751  
 Forbes, D.A., Georgakakis, A.E., & Brodie, J.P. 2001, *MNRAS*, 325, 1431  
 Gomez, M. & Richtler, T. 2004, *A&A*, 415, 499  
 Goudfrooij, P., Strader, J., Breneman, L., Kissler-Patig, M., Minniti, D., Huizinga, E. 2003, *MNRAS*, 343, 665  
 Harris, G.L.H., Harris, W.E., & Geisler, D. 2004, *AJ*, 128, 723  
 Harris, H.C., Hesser, J.E., Bothun, G.D., Hanes, D.A., & Harris, W.E. 1985, *AJ*, 90, 2495  
 Harris, W.E. 1981, *ApJ*, 251, 497  
 Harris, W.E. 1996, *AJ*, 112, 1487  
 Harris, W.E. & van den Bergh, S. 1981, *AJ*, 86, 1627  
 Hughes, S.M.G., et al. 1998, *ApJ*, 501, 32  
 Kissler-Patig, M., Ashman, K.M., Zepf, S.E., & Freeman, K.C. 1999, *AJ*, 118, 197  
 Kundu, A. & Whitmore, B.C. 2001, *AJ*, 121, 2950  
 Kundu, A., Whitmore, B.C., Sparks, W.B., & Macchetto, F.D. 1999, *ApJ*, 513, 733  
 Kundu, A. & Zepf, S.E. 2007, *ApJ*, 660, L109  
 Lacey, C. & Cole, S. 1993, *MNRAS*, 262, 627  
 Landolt, A.U. 1992, *AJ*, 104, 340  
 Mendez, R.A., Platais, I., Girard, T.M., Kozhurina-Platais, V., & van Altena, W.F. 2000, *AJ*, 119, 813  
 Mendez, R.A. & van Altena, W.F. 1996, *AJ*, 112, 655  
 Peng, E.W., Jordan, A., Cote, P., Blakeslee, J.P., Ferrarese, L., Mei, S., West, M.J., Merritt, D., Milosavljevic, M., Tonry, J.L. 2006, *ApJ*, 639, 95  
 Perrett, K.M., Bridges, T.J., Hanes, D.A., Irwin, M.J., Brodie, J.P., Carter, D., Huchra, J.P., & Watson, F.G. 2002, *AJ*, 123, 2490  
 Press, W.H. & Schechter, P. 1974, *ApJ*, 187, 425  
 Rhode, K.L. & Zepf, S.E. 2001, *AJ*, 121, 210  
 Rhode, K.L. & Zepf, S.E. 2003, *AJ*, 126, 2307  
 Rhode, K.L. & Zepf, S.E. 2004, *AJ*, 127, 302  
 Rhode, K.L., Zepf, S.E., & Santos, M.R. 2005, *ApJ*, 630, L21  
 Santos, M.R. 2003, in *Extragalactic Globular Cluster Systems*, ed. M. Kissler-Patig (New York: Springer-Verlag)  
 Schlegel, D.J., Finkbeiner, D.P., & Davis, M. 1998, *ApJ*, 500, 525  
 Searle, L. & Zinn, R. 1978, *ApJ*, 225, 357  
 Shapley, H. 1918, *ApJ*, 48, 154  
 Strader, J., Beasley, M., & Brodie, J.P. 2007, *AJ*, 133, 2015  
 Tonry, J.L., Blakeslee, J.P., Ajhar, E.A., Fletcher, A.B., Luppino, G.A., Metzger, M.R., & Moore, C.B. 2001, *ApJ*, 546, 681  
 Vesperini, E. 2000, *MNRAS*, 318, 841  
 Zepf, S.E. 2007, in *Globular Clusters: Guides to Galaxies*, ed. T. Richtler, in press  
 Zepf, S.E., & Ashman, K.M. 1993, *MNRAS*, 264, 611  
 Zepf, S.E. & Silk, J. 1996, *ApJ*, 466, 114  
 Zinn, R. 1985, *ApJ*, 293, 424

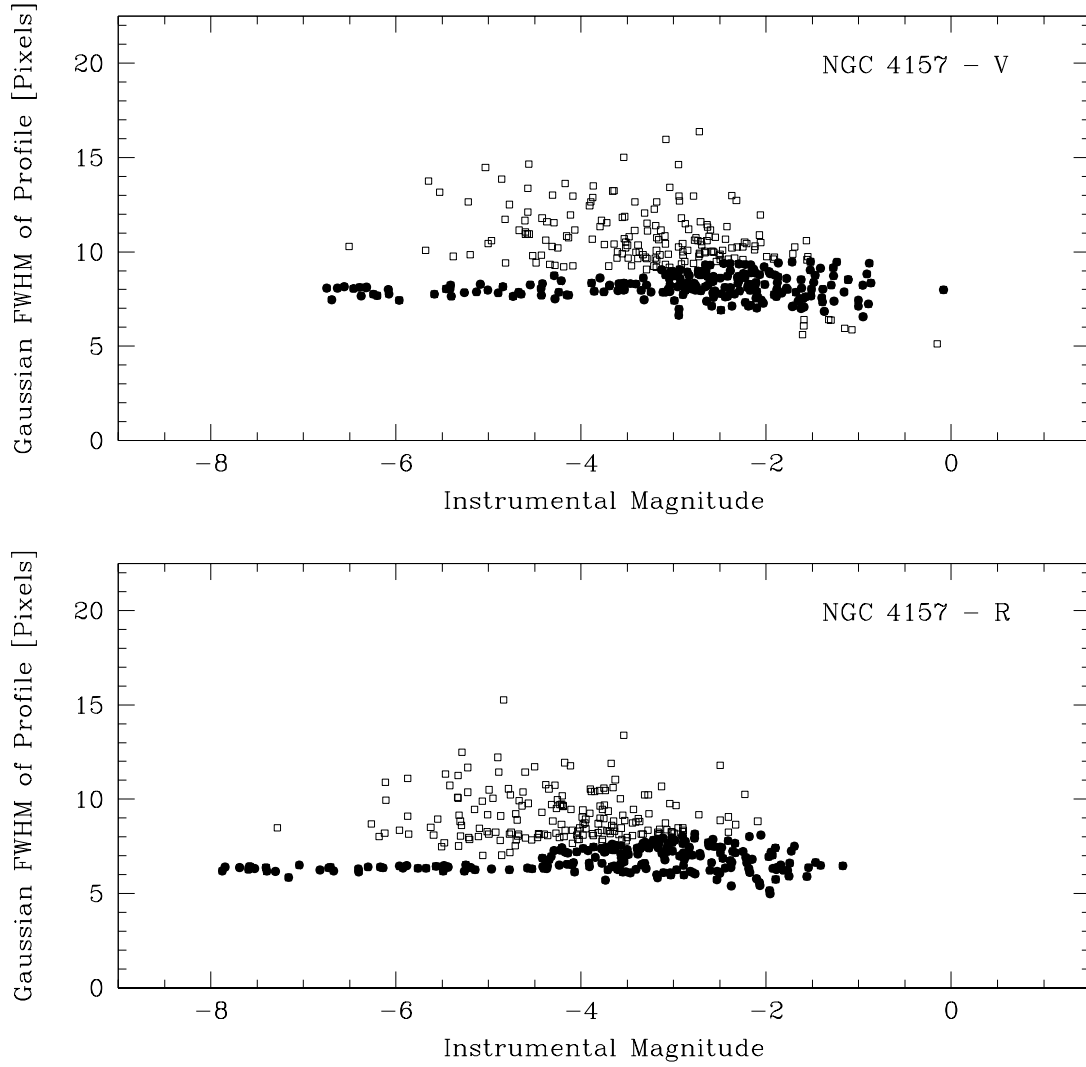


FIG. 1.— Gaussian FWHM of the radial profile vs. instrumental magnitude for 387 objects in the WIYN  $V$  and  $R$  images of NGC 4157. Filled circles are objects that pass the FWHM criteria; open squares are those that are not likely to be point sources and are therefore excluded as GC candidates.

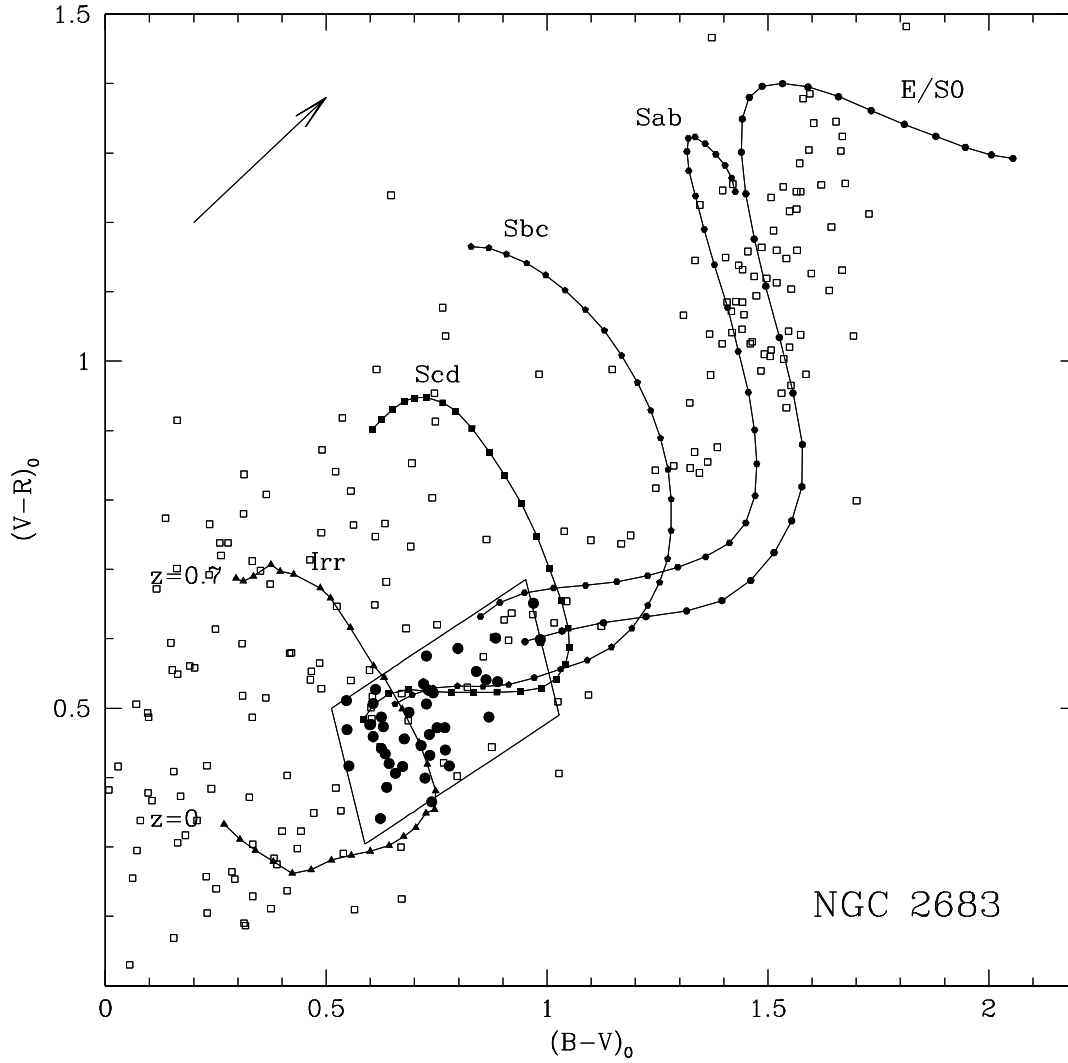


FIG. 2.— Color selection of GC candidates in NGC 2683. Open squares are the 271 point sources detected in all three filters; filled circles are the final set of 41 GC candidates. For reference, the locations in the  $BVR$  color-color plane of galaxies of various types are shown as tracks the galaxies would follow with increasing redshift. RZ01 details how the tracks were produced. A reddening vector of length  $A_V = 1$  mag appears in the upper left-hand corner.

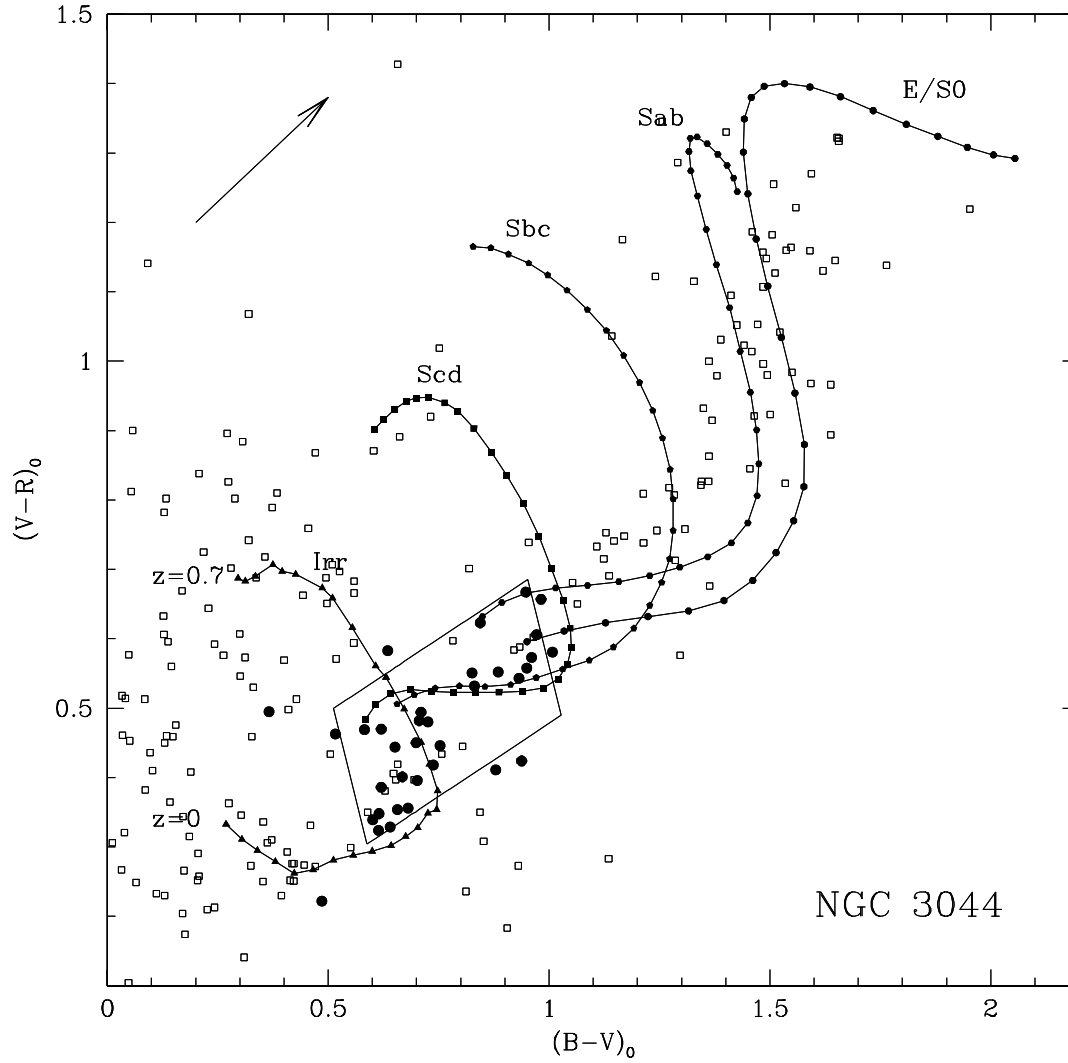


FIG. 3.— Color selection of GC candidates in NGC 3044. Open squares are the 262 point sources detected in all three filters; filled circles are 35 sources with  $V$  magnitudes and  $BVR$  colors like globular clusters. Note that only these 35 objects are spread uniformly over the entire WIYN image, and in Section 3.4 we argue that we have not convincingly detected this galaxy’s GC system.

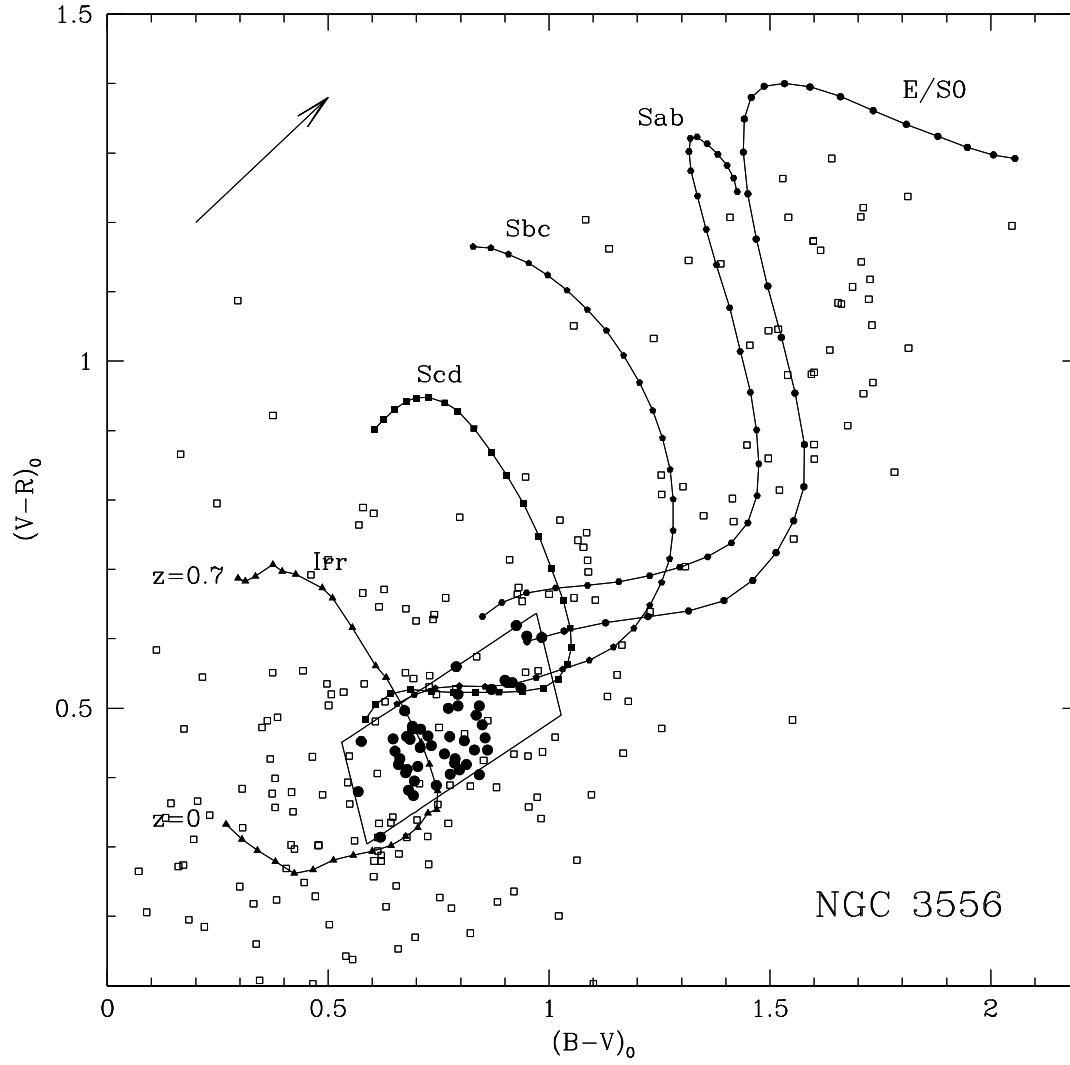


FIG. 4.— Color selection of GC candidates in NGC 3556. Open squares are the 275 point sources detected in all three filters; filled circles are the final set of 50 GC candidates.



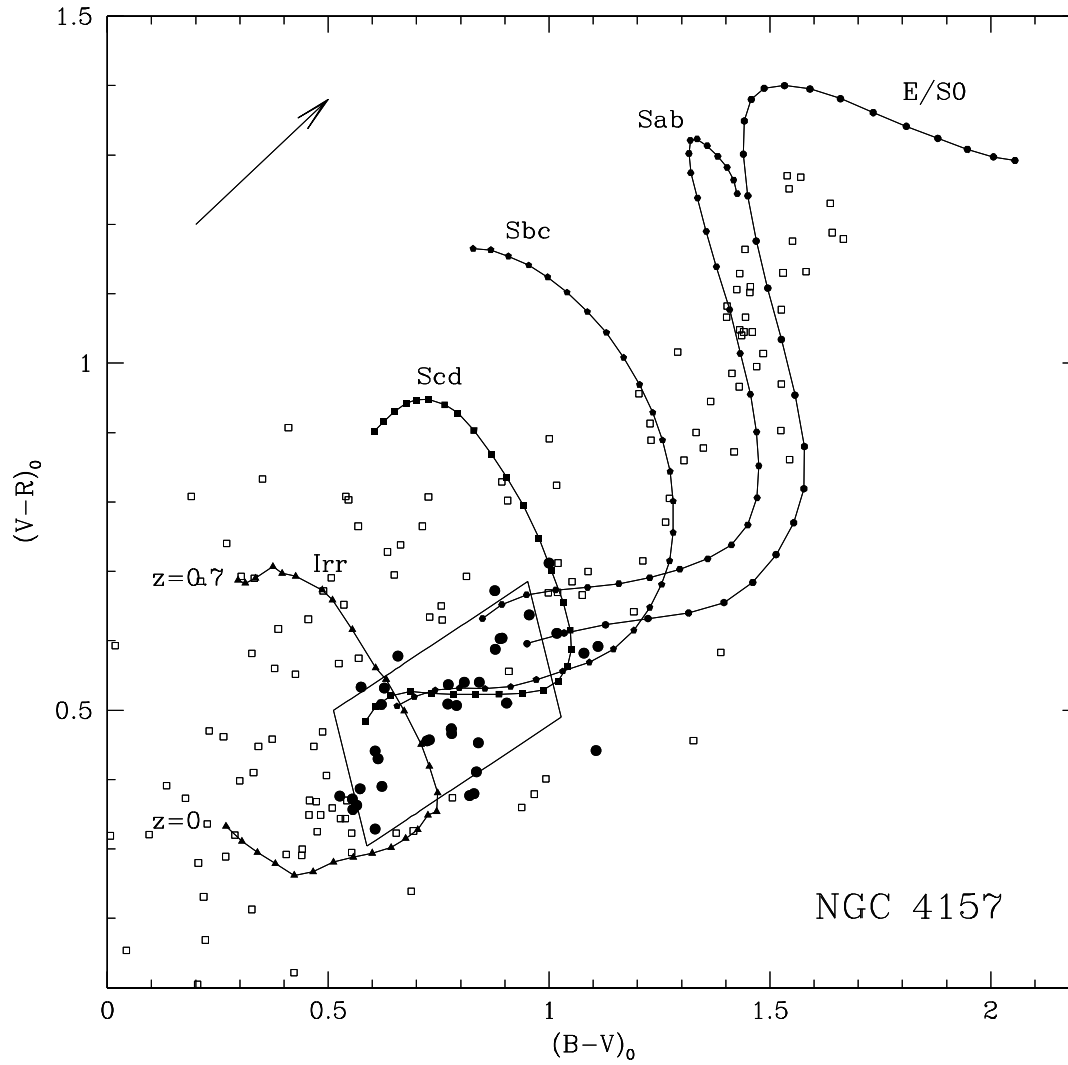


FIG. 5.— Color selection of GC candidates in NGC 4157. Open squares are the 171 point sources detected in all three filters; filled circles are the final set of 37 GC candidates.

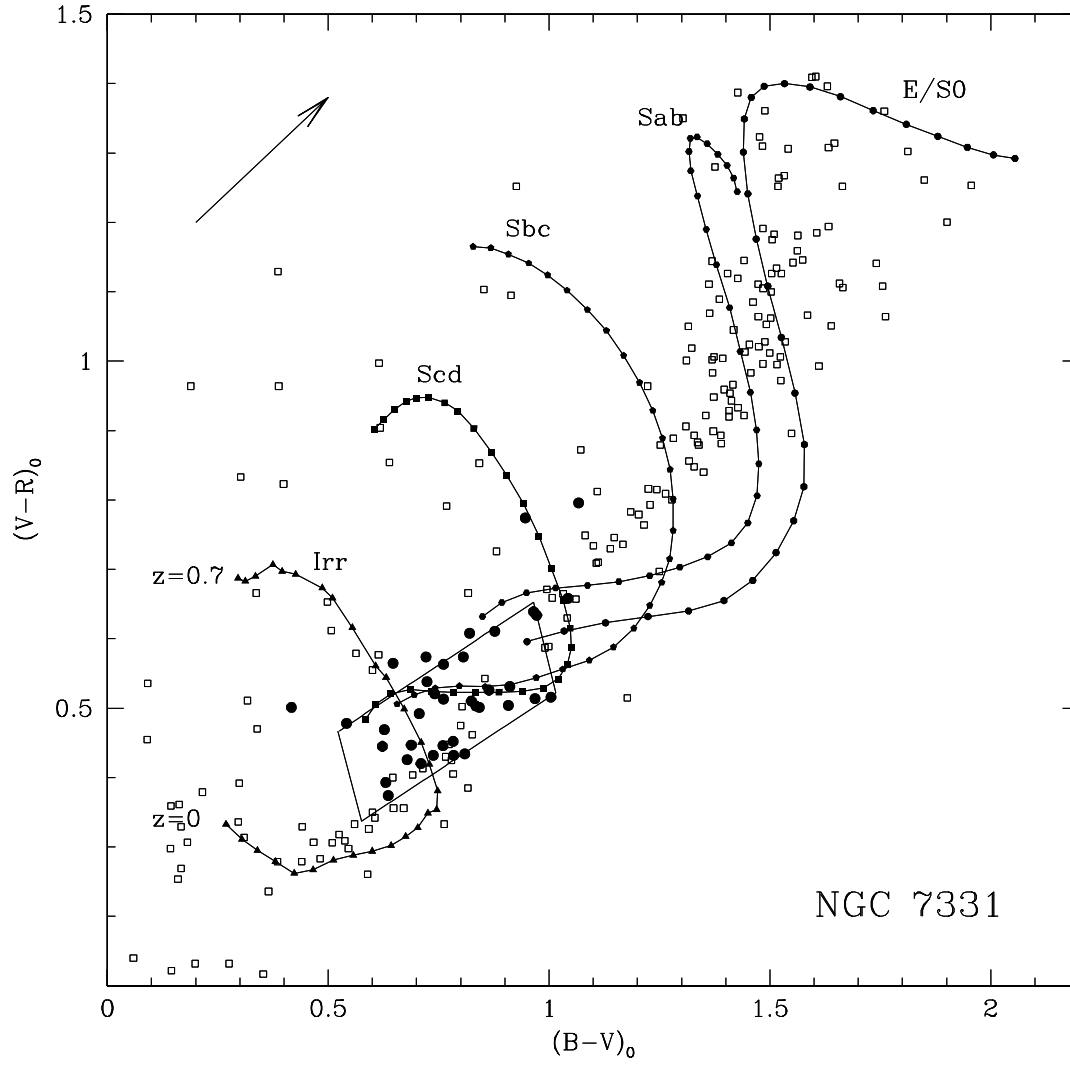


FIG. 6.— Color selection of GC candidates in NGC 7331. Open squares are the 245 point sources detected in all three filters; filled circles are the final set of 37 GC candidates.

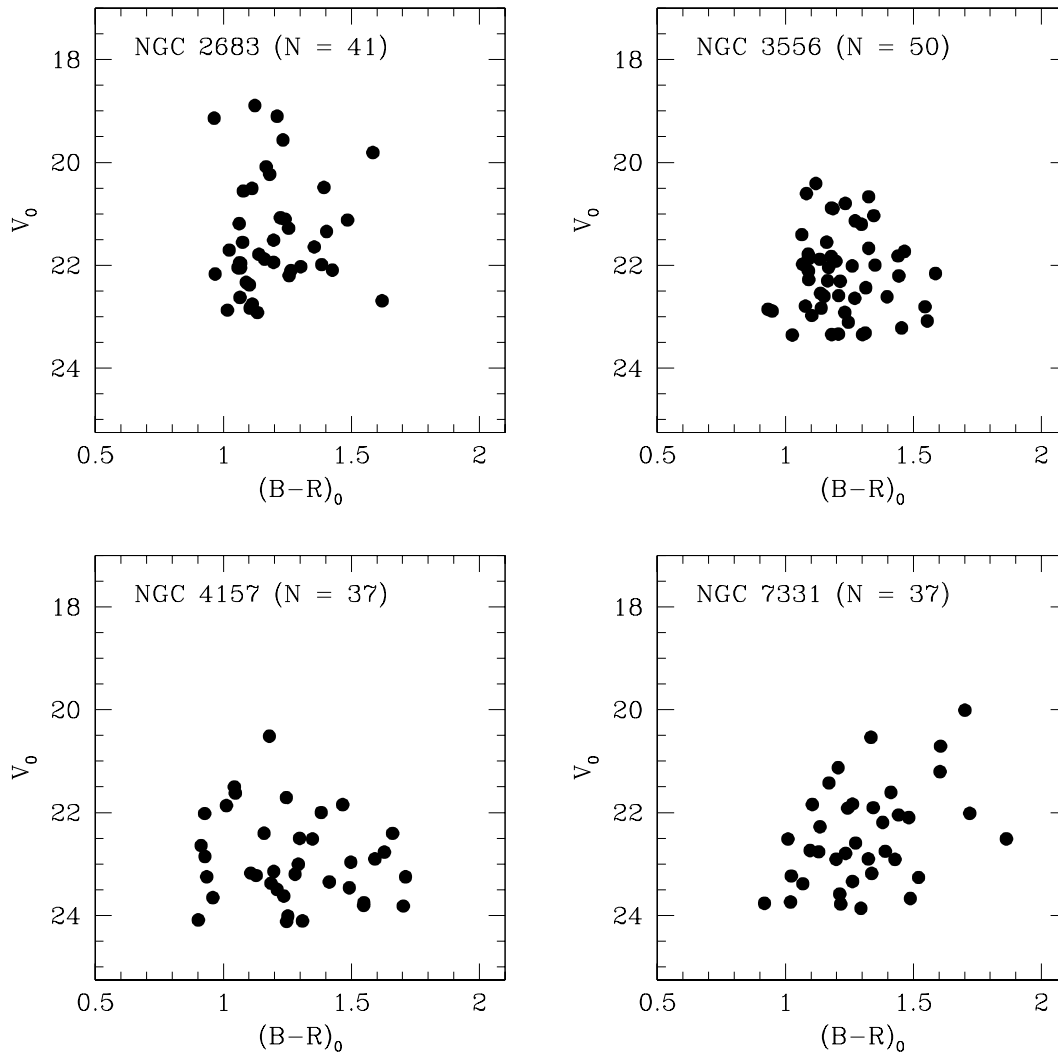


FIG. 7.—  $V$  versus  $B-R$  color-magnitude diagrams for the GC candidates found in each of the four galaxies in which the GC system was detected. The magnitudes and colors have been corrected for Galactic extinction in the direction of the target galaxies, but not for absorption internal to the galaxies.

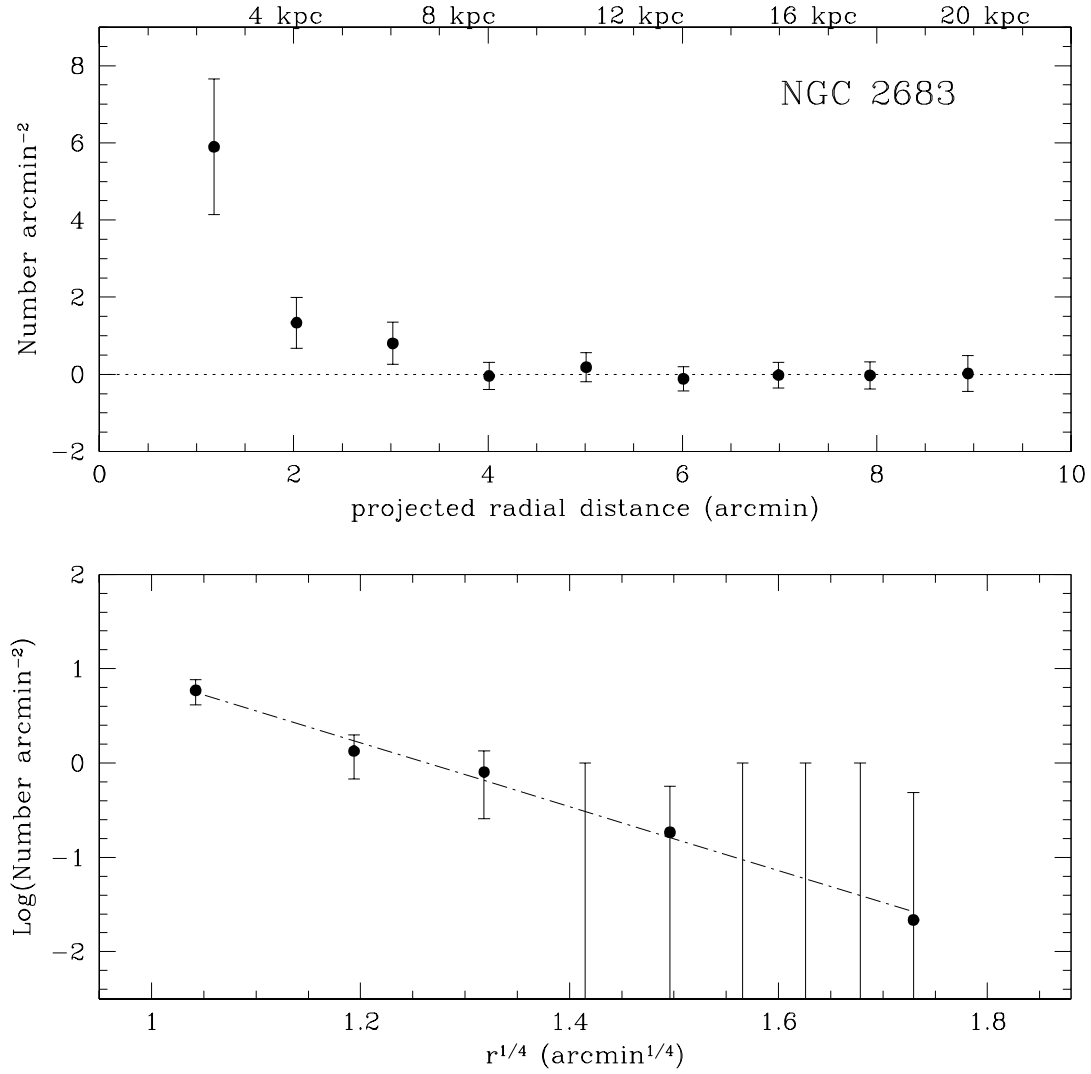


FIG. 8.— Radial distribution of GCs in NGC 2683, plotted as surface density vs. projected radial distance (top) and as the log of the surface density vs.  $r^{1/4}$  (bottom). The horizontal line in the top panel indicates a surface density of zero. The dashed line in the bottom panel is the best-fit de Vaucouleurs law. The data have been corrected for contamination, areal coverage, and magnitude incompleteness, as described in Section 4.1.

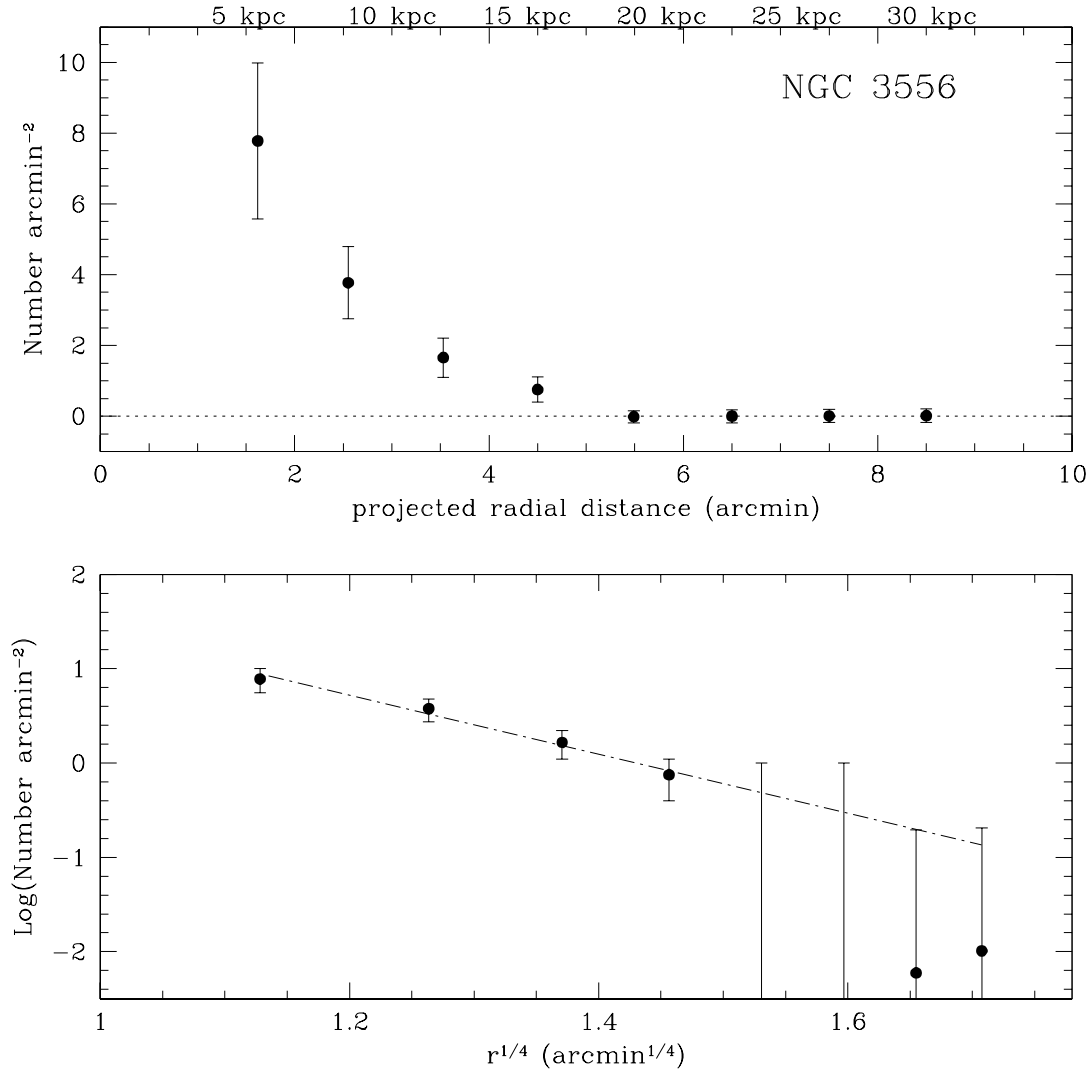


FIG. 9.— Radial distribution of GCs in NGC 3556, plotted the same way as in Fig. 8.

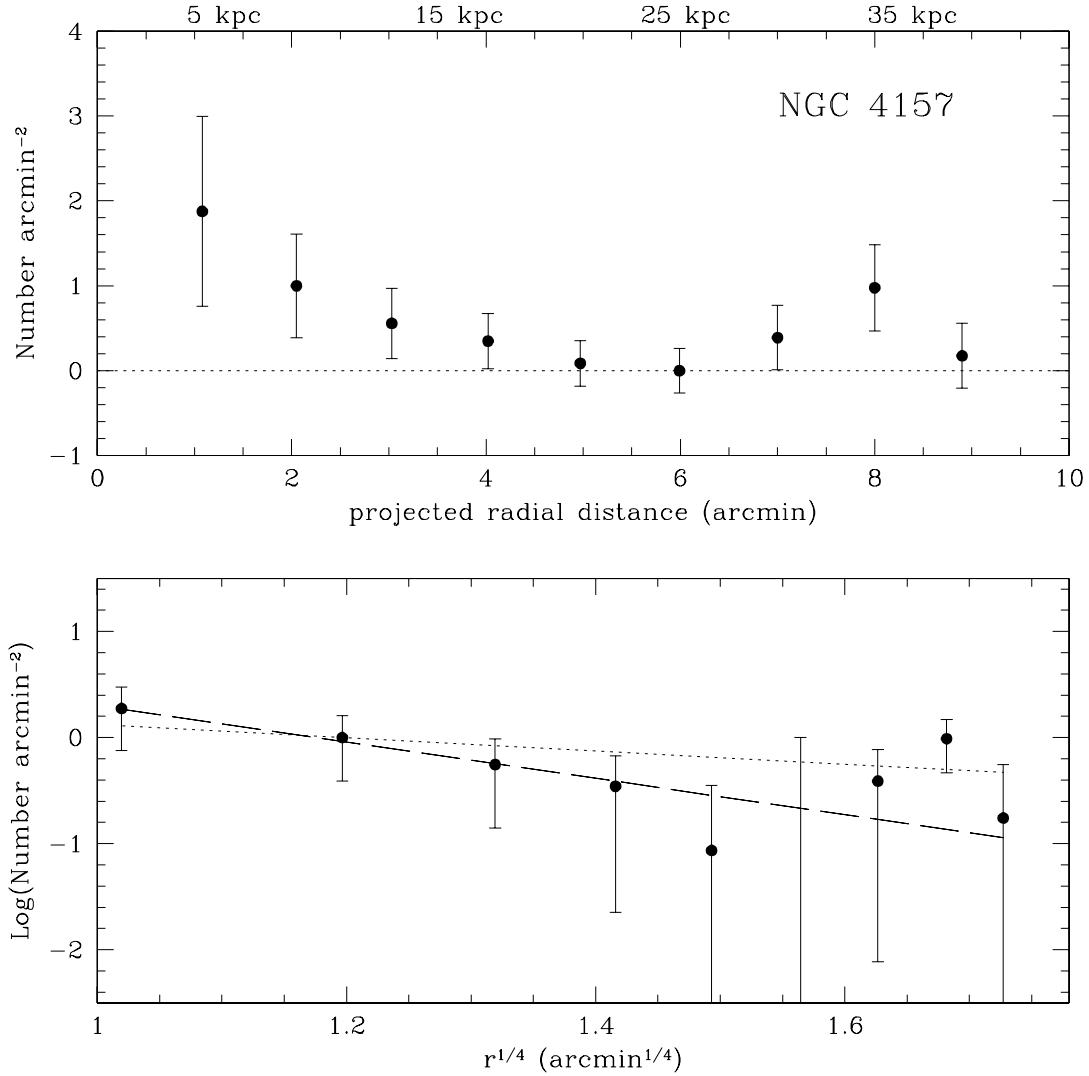


FIG. 10.— Radial distribution of GCs in NGC 4157, showing the surface density vs. projected radius in the top panel and the log of the surface density vs.  $r^{1/4}$  in the bottom panel. There is a spike in the surface density in the 7–8' bins, due to the presence of seven loosely-grouped objects that may or may not be real GCs in NGC 4157's halo. The dotted line in the bottom panel is the best-fit deVaucouleurs law with those seven objects included in the data; the dashed line is the deVaucouleurs law fit with the seven objects removed.

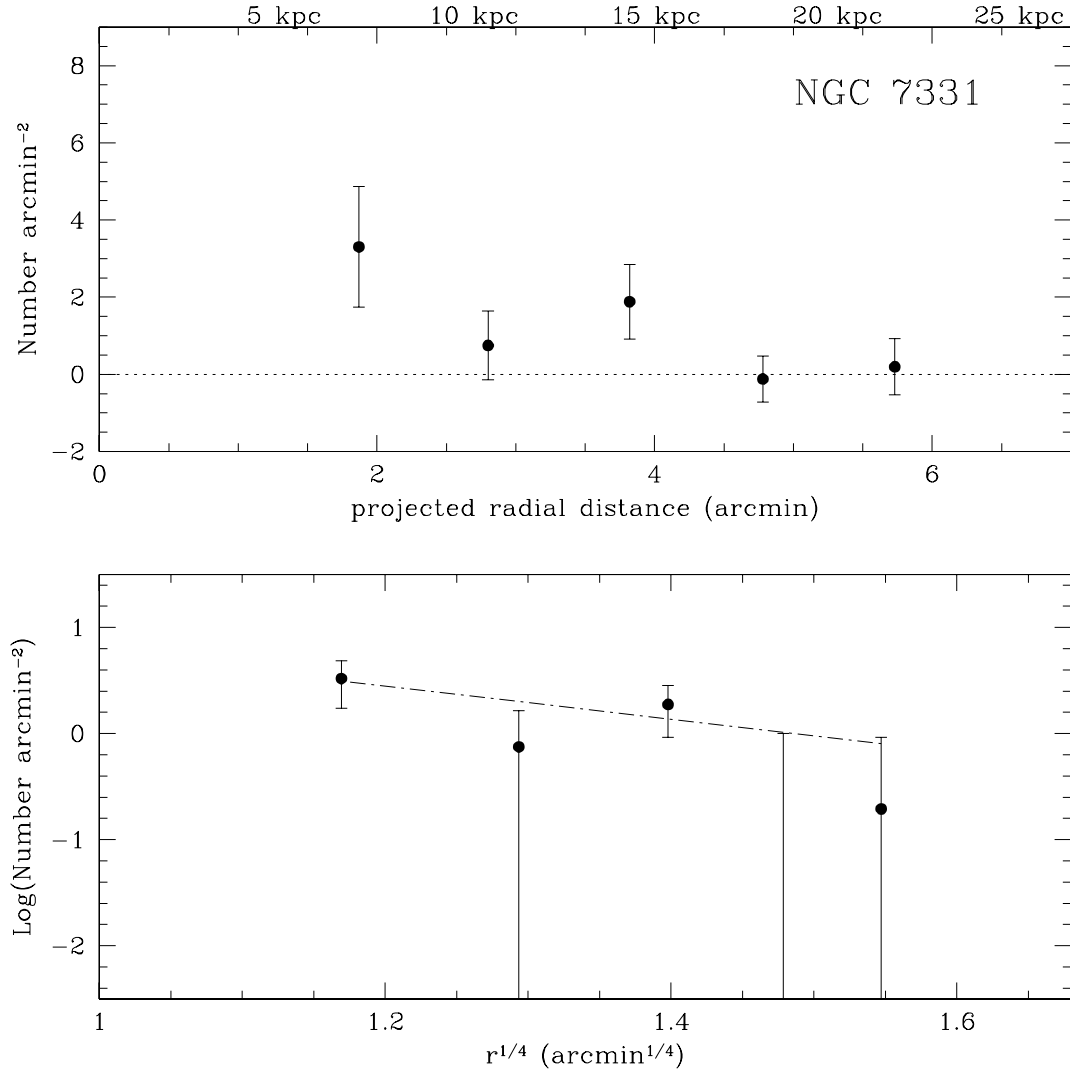


FIG. 11.— Radial distribution of GCs in NGC 7331, plotted the same way as in Fig. 8.

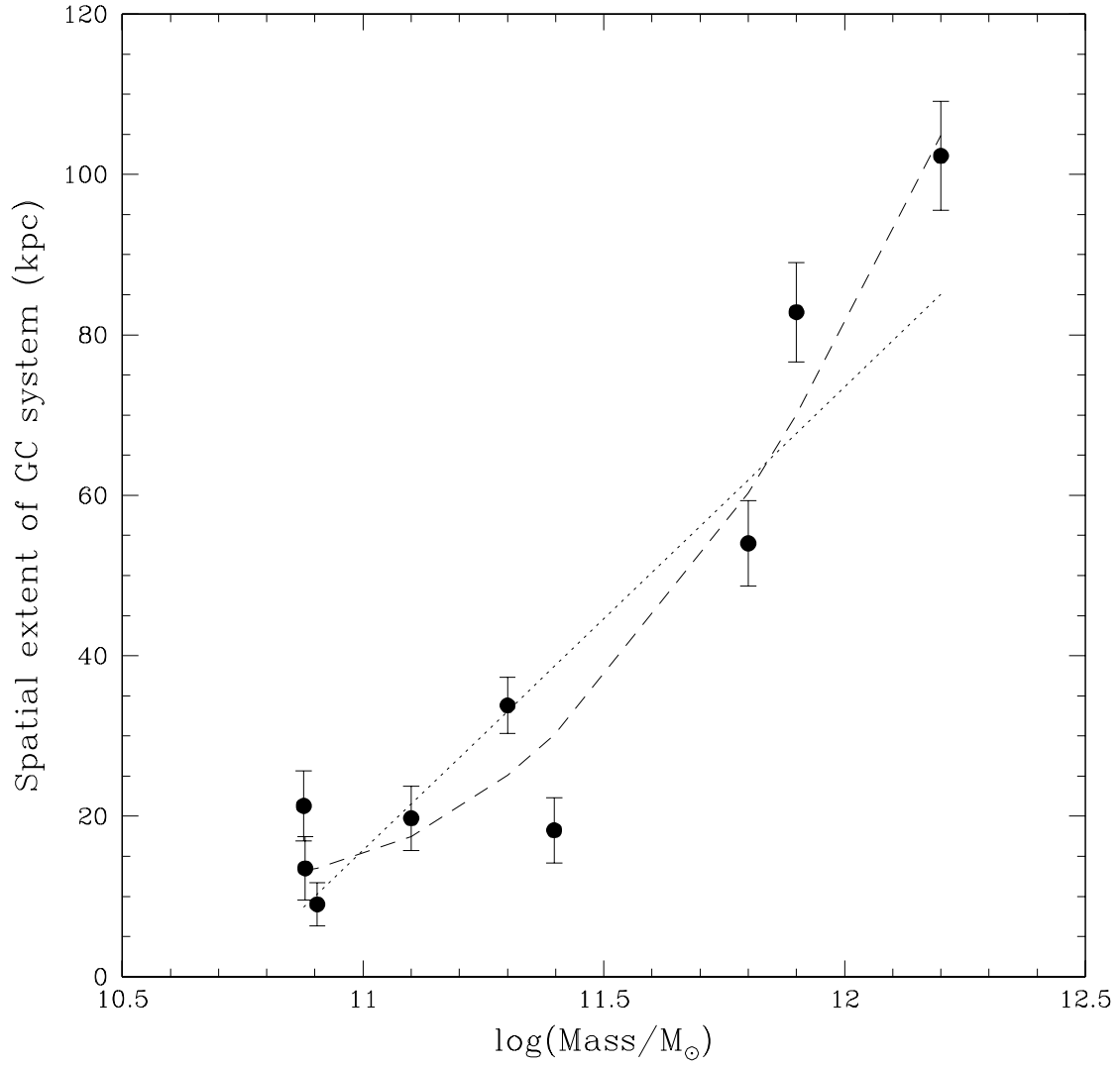


FIG. 12.— Radial extent of the globular cluster system in kiloparsecs versus the log of the galaxy mass in solar masses for nine elliptical, S0, and spiral galaxies included in our wide-field GC system survey to date. The best-fit line and second-order polynomial are shown as dotted and dashed lines, respectively.



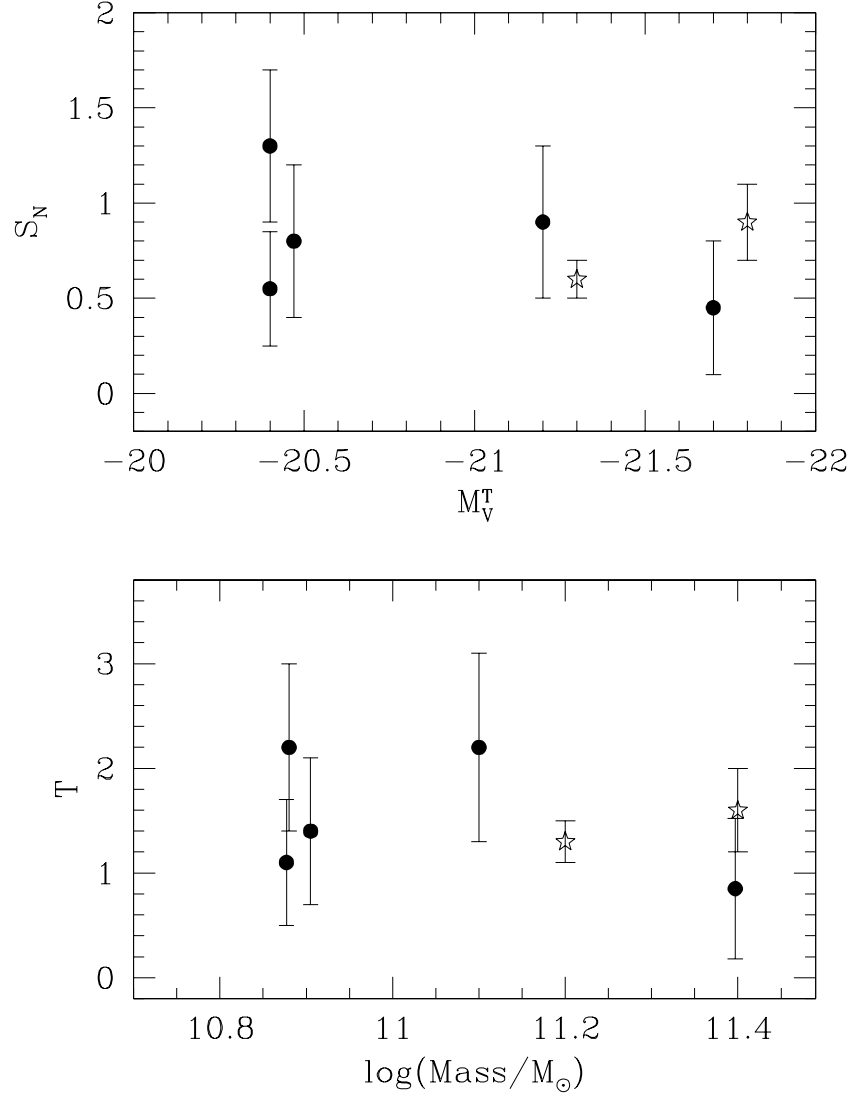


FIG. 13.— Luminosity-normalized specific frequency ( $S_N$ ) and mass-normalized specific frequency ( $T$ ) for the five spiral galaxies (four presented here and one presented in RZ03) analyzed for our wide-field GC system survey, plotted with filled circles. Specific frequencies of the GC systems of the Milky Way (smallest error bars) and M31 are plotted with open stars. The specific frequencies for the targeted spiral galaxies fall within a modest range and are consistent with the values for the Milky Way and M31.

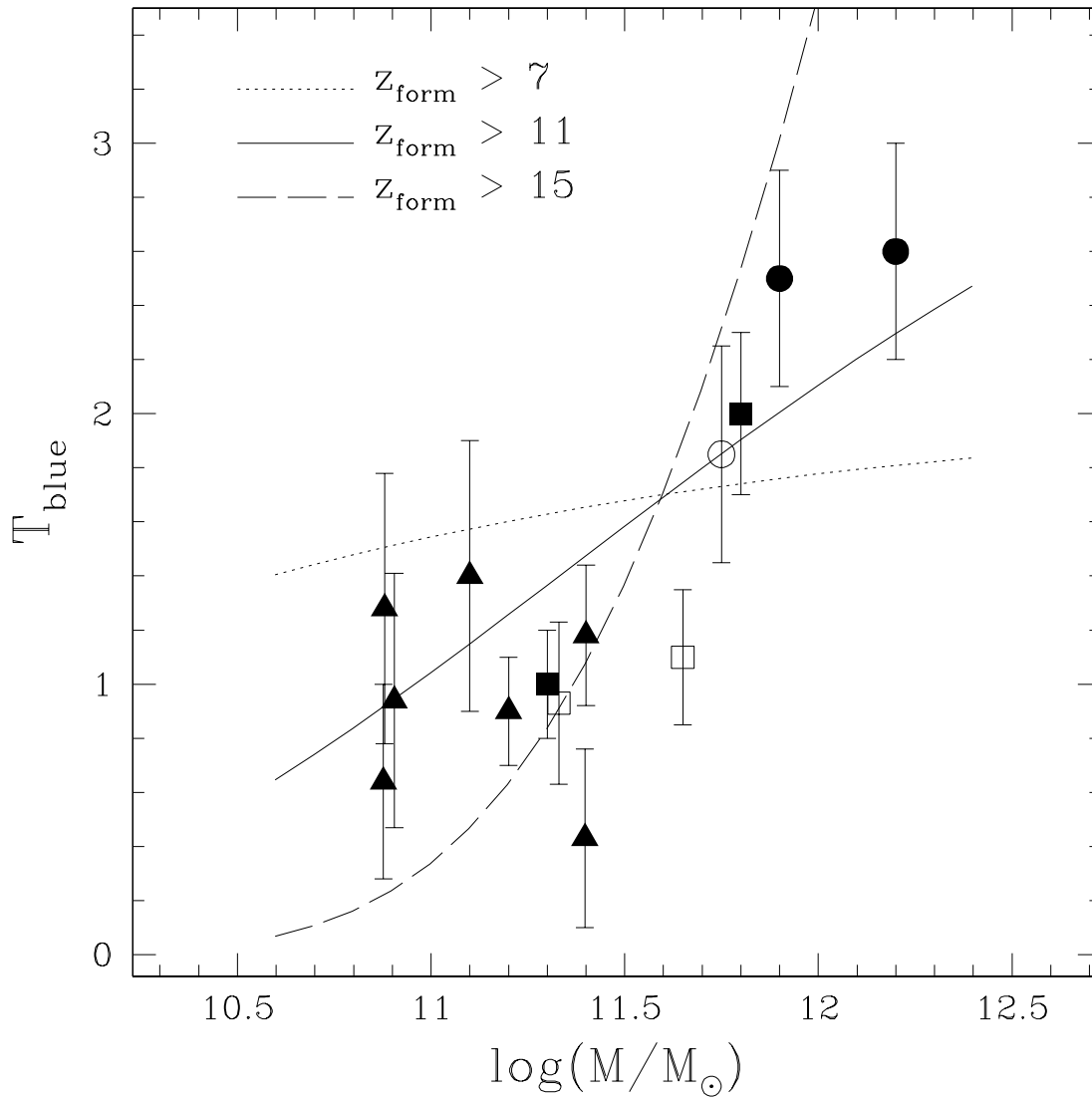


FIG. 14.— Number of blue GCs normalized by host galaxy stellar mass vs. the log of the galaxy stellar mass for 14 galaxies. Circles are cluster elliptical galaxies, squares are E/S0 field galaxies, and triangles are field spiral galaxies. Filled symbols denote the nine galaxies from our wide-field survey, as well as the Milky Way and M31. Open symbols are galaxies from other studies. The curves (courtesy of G. Bryan) show the expected trend if metal-poor GCs are formed prior to  $z$  of 7, 11, or 15, and assuming that the number of GCs is proportional to the fraction of the galaxy mass that has assembled prior to that redshift.

TABLE 1  
 BASIC PROPERTIES OF THE TARGET GALAXIES

Name	Type	$m - M$	Distance (Mpc)	$M_V^T$
NGC 2683	Sb	29.44	7.7	-20.5
NGC 3044	Sc	31.83	23.2	-21.0
NGC 3556	Sc	30.46	7.1	-21.2
NGC 4157	Sb	30.84	14.7	-20.4
NGC 7331	Sb	30.59	13.1	-21.7

NOTE. — Distances to NGC 2683, NGC 4157, and NGC 7331 are from Tonry et al. (2001) (surface brightness fluctuations). Distances to NGC 3044 and NGC 3556 are from combining the recession velocity with respect to the cosmic microwave background from RC3 (deVaucouleurs et al. 1991) with  $H_0 = 70 \text{ km s}^{-1} \text{ Mpc}^{-1}$ . Magnitudes are from combining  $V_T^0$  from RC3 (deVaucouleurs et al. 1991) with  $m - M$ .

 TABLE 2  
 WIYN OBSERVATIONS OF TARGET GALAXIES

Galaxy	Date	Detector	Exposure Times (seconds)		
			<i>B</i>	<i>V</i>	<i>R</i>
NGC 2683	Jan 2001	Minimosaic	3 x 2100	3 x 2000	3 x 1500
NGC 3044	Jan 2000	Minimosaic	3 x 1800	3 x 1800	3 x 1800
NGC 3556	Apr 2000	Minimosaic	3 x 2100	4 x 2000	3 x 1500
NGC 4157	Jan 2000	Minimosaic	3 x 1800	3 x 1500	3 x 1500
NGC 7331	Oct 1999	S2KB	3 x 1800	3 x 1800	3 x 1500

 TABLE 3  
 APERTURE CORRECTIONS USED FOR PHOTOMETRY OF SOURCES IN WIYN IMAGES

	NGC 2683	NGC 3044	NGC 3556	NGC 4157	NGC 7331
<i>B</i> .....	$-0.234 \pm 0.002$	$-0.290 \pm 0.003$	$-0.343 \pm 0.009$	$-0.278 \pm 0.009$	$-0.267 \pm 0.003$
<i>V</i> .....	$-0.294 \pm 0.004$	$-0.224 \pm 0.004$	$-0.270 \pm 0.006$	$-0.206 \pm 0.007$	$-0.353 \pm 0.003$
<i>R</i> .....	$-0.152 \pm 0.003$	$-0.124 \pm 0.004$	$-0.230 \pm 0.005$	$-0.280 \pm 0.007$	$-0.330 \pm 0.002$

 TABLE 4  
 EXTINCTION CORRECTIONS USED FOR PHOTOMETRY OF SOURCES IN WIYN IMAGES

	NGC 2683	NGC 3044	NGC 3556	NGC 4157	NGC 7331
$A_B$ .....	0.140	0.108	0.068	0.091	0.394
$A_V$ .....	0.108	0.084	0.055	0.069	0.303
$A_R$ .....	0.087	0.068	0.042	0.057	0.245

TABLE 5  
50% COMPLETENESS LIMITS OF WIYN IMAGES

	NGC 2683	NGC 3556	NGC 4157	NGC 7331
<i>B</i> .....	25.2	25.0	24.5	24.8
<i>V</i> .....	24.8	24.7	24.3	24.6
<i>R</i> .....	24.6	24.7	23.6	24.1

TABLE 6  
HST WFPC2 OBSERVATIONS ANALYZED FOR THIS STUDY

Proposal ID	Target Name	Exp Time (sec)	Ang Sep (')	Filter
NGC 2683:				
5446	NGC 2683	160	0.7	F606W
8199	NGC 2683	2600	1.9	F814W
NGC 3556:				
5446	NGC 3556	160	0.4	F606W
NGC 7331:				
5397/6294	NGC 7331	40400	3.5	F555W
5397/6294	NGC 7331	9600	3.5	F814W
8805	Any	2500	5.2	F606W

TABLE 7  
CORRECTED RADIAL PROFILE OF  
THE GC SYSTEM OF NGC 2683

Radius (arcmin)	Surface Density (arcmin <sup>-2</sup> )
1.2	5.90 ± 1.75
2.0	1.34 ± 0.66
3.0	0.80 ± 0.54
4.0	-0.04 ± 0.35
5.0	0.18 ± 0.38
6.0	-0.12 ± 0.32
7.0	-0.02 ± 0.33
7.9	-0.03 ± 0.36
8.9	0.02 ± 0.46

TABLE 8  
CORRECTED RADIAL PROFILE OF  
THE GC SYSTEM OF NGC 3556

Radius (arcmin)	Surface Density (arcmin <sup>-2</sup> )
1.6	7.78 ± 2.21
2.6	3.77 ± 1.02
3.5	1.66 ± 0.56
4.5	0.75 ± 0.35
5.5	-0.02 ± 0.17
6.5	0.00 ± 0.18
7.5	0.01 ± 0.19
8.5	0.01 ± 0.19

TABLE 9  
CORRECTED RADIAL PROFILE OF THE GC  
SYSTEM OF NGC 4157

Radius (arcmin)	Surface Density (arcmin <sup>-2</sup> )
1.1	1.88 ± 1.12
2.1	1.00 ± 0.61
3.0	0.56 ± 0.42
4.0	0.35 ± 0.33
5.0	0.09 ± 0.27
6.0	0.00 ± 0.26
7.0	0.39 ± 0.38 (0.20 ± 0.33)
8.0	0.98 ± 0.51 (-0.16 ± 0.21)
8.9	0.17 ± 0.38

NOTE. — Values in parentheses are the surface density when the seven loosely-grouped GC candidates located in the galaxy's outer halo is removed.

TABLE 10  
CORRECTED RADIAL PROFILE OF THE GC  
SYSTEM OF NGC 7331

Radius (arcmin)	Surface Density (arcmin <sup>-2</sup> )
1.9	3.30 ± 1.57
2.8	0.75 ± 0.89
3.8	1.88 ± 0.96
4.8	-0.12 ± 0.60
5.7	0.19 ± 0.73

TABLE 11  
COEFFICIENTS FROM FITTING RADIAL PROFILE DATA

Galaxy	deVaucouleurs Law		Power Law	
	a0	a1	a0	a1
NGC 2683	$4.28 \pm 0.77$	$-3.39 \pm 0.68$	$0.93 \pm 0.13$	$-2.35 \pm 0.47$
NGC 3556	$4.48 \pm 0.66$	$-3.13 \pm 0.52$	$1.43 \pm 0.17$	$-2.27 \pm 0.38$
NGC 4157 †	$0.74 \pm 0.50$	$-0.62 \pm 0.35$	$0.16 \pm 0.17$	$-0.51 \pm 0.27$
	$2.02 \pm 0.67$	$-1.71 \pm 0.53$	$0.34 \pm 0.18$	$-1.27 \pm 0.39$
NGC 7331	$2.33 \pm 1.28$	$-1.57 \pm 0.99$	$0.81 \pm 0.34$	$-1.16 \pm 0.74$

† The first set of coefficients for NGC 4157 is for fits to the radial profile data including a group of seven GC candidates in the galaxy’s halo; the second set is for fits to the profile with those seven candidates removed.

TABLE 12  
RADIAL EXTENTS OF GC SYSTEMS OF SURVEY GALAXIES

Galaxy	Mass [ $\log(M/M_{\odot})$ ]	GC System Extent (kpc)	Reference
NGC 2683	10.9	$9 \pm 3$	4
NGC 3379	11.3	$34 \pm 4$	3
NGC 3556	11.1	$20 \pm 4$	4
NGC 4157	10.9	$21 \pm 4$	4
NGC 4406	11.9	$83 \pm 6$	3
NGC 4472	12.2	$102 \pm 7$	1
NGC 4594	11.8	$54 \pm 5$	3
NGC 7331	11.4	$18 \pm 4$	4
NGC 7814	10.9	$13 \pm 4$	2

REFERENCES. — (1) Rhode & Zepf 2001; (2) Rhode & Zepf 2003; (3) Rhode & Zepf 2004; (4) this paper.

TABLE 13  
TOTAL NUMBERS AND SPECIFIC FREQUENCIES OF GC SYSTEMS

Galaxy	$N_{GC}$	$S_N$	$T$	$T_{\text{blue}}$
NGC 2683	$120 \pm 40$	$0.8 \pm 0.4$	$1.4 \pm 0.7$	$0.9 \pm 0.5$
NGC 3556	$290 \pm 80$	$0.9 \pm 0.4$	$2.2 \pm 0.9$	$1.4 \pm 0.5$
NGC 4157	$80 \pm 20$	$0.6 \pm 0.3$	$1.1 \pm 0.6$	$0.6 \pm 0.4$
NGC 7331	$210 \pm 130$	$0.5 \pm 0.4$	$0.9 \pm 0.7$	$0.4 \pm 0.3$